공학석사학위논문

HILS Verification of Low Earth Orbit Cube-Satellite Attitude Determination and Control System Using Helmholtz Cage

헬름홀츠 케이지를 이용한 저궤도 큐브위성 자세결정 및 제어시스템의 HILS 검증

2019년 2월

서울대학교 대학원

기계항공공학부

심 한 준

HILS Verification of Low Earth Orbit Cube-Satellite Attitude Determination and Control System Using Helmholtz Cage

헬름홀츠 케이지를 이용한 저궤도 큐브위성 자세결정 및 제어시스템의 HILS 검증

지도교수 기 창 돈

이 논문을 공학석사 학위논문으로 제출함

2019 년 2 월

서울대학교 대학원

기계항공공학부

심 한 준

심한준의 공학석사 학위논문을 인준함

2018 년 12 월

위 원 장 김 유 단

부위원장 기 창 돈

위 원 김 현 진

Abstract

HILS Verification of Low Earth Orbit Cube-Satellite Attitude Determination and Control System Using Helmholtz Cage

Hanjoon Shim
School of Mechanical and Aerospace Engineering
The Graduate School
Seoul National University

In this thesis, Hardware-In-the-Loop Simulation (HILS) verification of attitude determination and control system (ADCS) is addressed for low earth orbit cube-satellite equipped with a magnetorquer only. Unlike ordinary satellites equipped with reaction wheels, only a magnetorquer is mounted on cube-satellite due to spatial constraints. It is a simple, low-weight, and low-power consumption actuator that enables efficient operation of cube-satellite and aims to maintain nadir-pointing control. In order to achieve the objective of the proposed system, firstly, the equations of motion for the cube-satellite is expressed in terms of the gravity gradient torque, and the input torque calculated from the dipole

moment of the magnetorquer and geomagnetic field. Then, a linear system model is obtained by interpreting the uncertainty flowing into the system as noise sources. In addition, extended Kalman filter equations are derived to estimate the attitude of the cube-satellite by defining the reference vector from the sun and magnetic field model, and fusing the sun sensor, magnetometer, and gyroscope measurements. Then, LQR controller can be designed to maintain nadir-pointing by calculating the optimal solution from the cost function composed of a given linear system and input. In order to verify the performance of the proposed system, HILS should be performed considering various constraints of the ground environment. However, it is difficult to verify the above-described system in a ground environment due to limitations in the performance of magnetorquer such as small input torque effected by the magnitude of the geomagnetic field, and decoupled input control.

So far, it has been studied that the verification of cube-satellite ADCS for the stabilization of angular velocity, the passive control method which depends on geomagnetic field alignment, and HILS using reaction wheels. HILS of ADCS using only magnetorquer also has been proposed, but the performance analysis was limited due to the constraints of the ground environment. In contrast, the proposed HILS is aimed at verifying magnetorquer mounted cube-satellite ADCS that solves the limitations from unknown error factors of the

ground environment. Therefore, in this thesis, HILS verification of cube-satellite ADCS using Helmholtz cage is proposed. It is focused on output characteristics proportional to the magnitude of the external magnetic field of the magnetorquer. In other words, it is solved by controlling the magnetic field vector generated from Helmholtz cage that is the degradation of the estimation performance due to the magnetic field including the statistical error characteristic in the indoor environment and the control performance deterioration due to the small input torque of the magnetorquer which is vulnerable to the disturbance. To construct a magnetic field vector from Helmholtz cage, it is designed using the Biot-Savat law to model the current-magnetic field relationship. Also, it is designed to have a size enough to ensure the magnetic field uniformity of the space including the cube-satellite. The magnetic field vector controller of Helmholtz cage can be easily designed by approximating the transfer function from the derived current-magnetic field equation and using the classical control technique. In this case, cube-satellite is suspended in the inner space of Helmholtz cage to perform single axis HILS verification of ADCS. Since the GPS measurement value cannot be calculated in the indoor experiment environment, the nadir-pointing reference vectors are redefined by the mean measurement values of the simulated sunlight and the magnetic field generated from Helmholtz cage. Then, by defining a coordinate system based on the

Helmholtz cage in the proposed HILS environment, nadir-pointing control performance can be expected by the computer simulation. Based on these simulation results, the proposed system can be verified by comparison with actual experimental results.

To demonstrate the validity of the proposed method, a single axis HILS verification of ADCS using SNUGLITE cube-satellite is presented. The proposed method can verify the performance of nadir-pointing control on the ground by using only the magnetorquer which is typically installed in cube-satellite. It is also confirmed that the estimation performance and the control reliability of ADCS can be verified effectively compared with the method which does not utilize Helmholtz cage. The proposed HILS verification technique is expected to be used for verification of cube-satellite ADCS for various tasks due to its simplicity and practicality.

Keywords: Cube-Satellite, Helmholtz Cage, Magnetorquer, Attitude Determination and Control System, Extended Kalman Filter, LQR Controller, Hardware-In-the-Loop Simulation(HILS)

Student Number: 2017-24667

Table of Contents

Nomenclature

m	= mass of the cube-satellite
I	= moment of inertia
M	= mass of the earth
R_e	= radius of the earth
n	= mean motion
g	= gravitational acceleration
G	= gravitational constant
μ_e	= gravitational parameter
μ_0	= permeability of free space
Ω_e	= rotation angle of the earth
i_h	= current of Helmholtz cage
K_{bdot}	= B-dot control constant
K_s	= current compensation constant
K_i	= integrator constant of Helmholtz cage
K_h	= modeling constant of Helmholtz cage
r_{ecef}	= position vector in ECEF
v_{ecef}	= velocity vector in ECEF
ϕ, θ, ψ	= Euler angles (roll, pitch, yaw)
p, q, r	= Angular velocity (roll, pitch, yaw)
τ_{gg}	= gravity gradient torque

τ_{str}	= string torque
τ_{mt}	= control input torque
σ_{gg}	= gravity gradient torque process noise
σ_{sr}	= solar radiation pressure torque process noise
σ_{ad}	= air drag torque process noise
σ_{mdt}	= residual dipole moment process noise
σ_{rrw}	= rate random walk process noise
σ_{sun}	= sun sensor measurement noise
σ_{mag}	= magnetometer measurement noise
σ_{arw}	= angular random walk measurement noise
$\mathbf{q} = \begin{bmatrix} q_0 & q_1 & q_2 & q_3 \end{bmatrix}^T$	= quaternion state
$\boldsymbol{\omega} = \begin{bmatrix} \omega_x & \omega_y & \omega_z \end{bmatrix}^T$	= angular velocity state
$\mathbf{b} = \begin{bmatrix} b_x & b_y & b_z \end{bmatrix}^T$	= gyro bias state
$\boldsymbol{\mu} = \begin{bmatrix} \mu_x & \mu_y & \mu_z \end{bmatrix}^T$	= dipole moment
$\mathbf{B}$	= geomagnetic vector in body frame
$\mathbf{B}_{meas}$	= magnetic measurement vector in body frame
$\mathbf{B}_{IGRF}$	= magnetic model vector in NED frame
$\mathbf{s}$	= sun vector in body frame
$\mathbf{s}_{meas}$	= sun measurement vector in body frame
$\mathbf{s}_{DE405}$	= solar system model vector in ECI frame

List of Figures

List of Tables

Chapter 1

Introduction

Cube-satellites are classified as nano-satellites with weights ranging from $1kg$ to less than $10kg$. In 1999, a standard size of 1U was defined as a cube with a length of $10cm$ on one side in CalPoly and Stanford University and cube-satellite which has single or multiple structure of 1U standard was proposed [1]. Because of its simplicity, low-weight, and the fact that it can be operated and developed at low-cost as compared with conventional satellites, over hundreds of cube-satellites have been developed and launched. Most cube-satellites have been developed for educational purpose and technology verification purposes. Due to the advantages of cube-satellite, it has been attempted to develop a scientific mission and communication for replacing the mission of the existing large satellites. However, in order to perform missions as large-sized satellites, the nadir-pointing control of cube-satellite is indispensable [2], [3]. In order to overcome the limitations of cube-satellite mission, the attitude determination and control system (ADCS) has been developed [4]-[11]. This thesis is an extension of the earlier work on the development and verification of ADCS for

cube-satellites. In this process, the development phase and verification for improving the performance of cube-satellite ADCS are introduced.

1.1. Brief Review of SNUGLITE Cube-Satellite Project

1.1.1. Introduction of SNUGLITE Cube-Satellite

SNUGLITE is a standard 2U cube-satellite developed by Seoul National University GNSS laboratory. It was launched in December 2018 from Falcon-9 launch vehicle on SSO-A. The orbit is a 575 kilometers sun-synchronous orbit. Its mission is to study prediction of an earthquake and ionospheric disturbances by collecting magnetic field and Total Electronic Contents (TEC) measurements from the extremely sensitive magnetometer and dual frequency GPS receivers. Since the mission data acquired during the operation period must be transmitted to the ground station, it is essential to maintain the nadir-pointing in order to carry out this mission successfully. In order to accomplish this mission, attitude determination and control system according to SNUGLITE operating scenario is configured as shown in Figure 1.1.

First, when a satellite is ejected from the P-Pod, it has an arbitrary angular velocity and angular velocity attenuation control is performed

to stabilize it. At this time, most cube satellites perform angular rate attenuation control for stability of battery charging and beacon transmission [2], [3]. Likewise, the mode for angular rate attenuation is performed in SNUGLITE. Another important aspect of angular velocity stabilization is ensuring a stable visible satellite of the GPS receiver. This is very important for ADCS because it defines the orbital coordinate system of SNUGLITE.

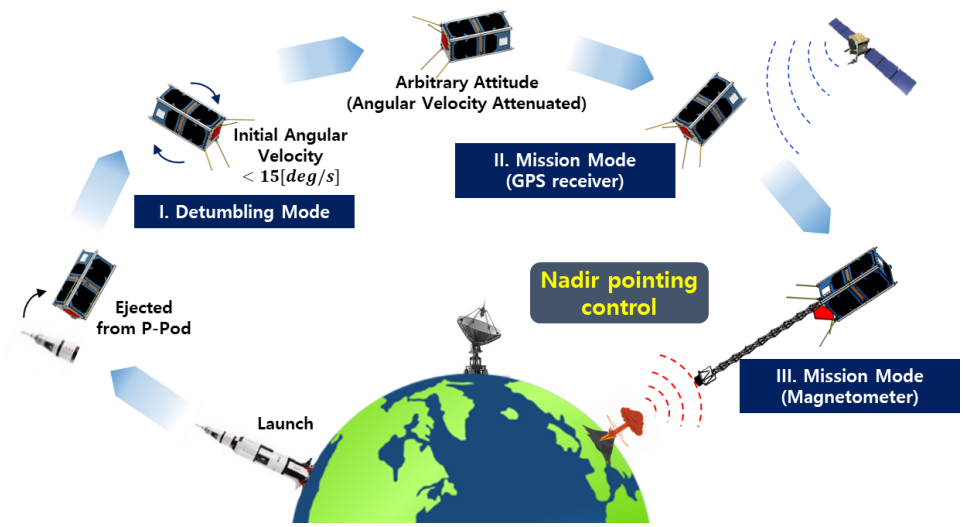

Figure 1.1: Operation Scenario of SNUGLITE Cube-Satellite

When the angular velocity is stabilized, SNUGLITE performs ADCS to maintain the nadir-pointing for mission execution. Then, the communication with the ground station will be started, and the GPS receiver will be verified firstly. After the receiver verification is

completed, the task of collecting the TEC measurement is performed. When a command from the ground station is given, the boom structure can be deployed and the precision magnetic field can be measured by the extremely sensitive magnetometer at the tip of boom structure. ADCS constructed in this thesis focuses on maintaining the nadir-pointing after the angular velocity stabilization for successful mission execution. Therefore, in this thesis, the performance verification of ADCS describes how accurately the nadir-pointing is maintained.

1.1.2. SNUGLITE Configuration

Most cube-satellite ADCS utilize a geomagnetic field for effective control at low-earth orbit. The most popular actuator is a geomagnetic field alignment actuator using passive control methods, followed by magnetometer. In addition, actuators such as reaction wheels and thrusters are used for the nadir-pointing, but these actuators are rarely used for cube-satellite. And the nadir-pointing cube-satellites are only about 15% of the total in Figure 1.2 [2], [3].

In the case of general large satellites, the reaction wheel and the thrusters are generally used to control the attitude for communication and mission performance. However, these actuators are not suitable for mounting on cube-satellite due to the spatial constraints.

Therefore, SNUGLITE chose an only magnetorquer as an actuator for cube-satellite focusing on space limitation and power efficiency [12]. As shown in Table 1, the magnetorquer has the advantage of being simple, low-weight, and low-power consumption, though there is a disadvantage that the input torque is small as compared with the actuator such as the reaction wheel and the thruster. Especially, it can be regarded as an actuator suitable for a cube-satellite having a limited size.

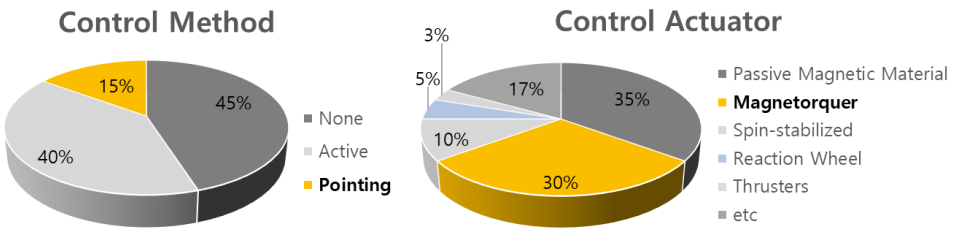

Figure 1.2: Statistics of Control Method and Actuator of Cube-satellite

Table 1.1: Comparison of Cube-satellite Contol Actuators

Features	Magnetorquer	Reaction Wheel	Thrusters
Torque	Low	High	High
Weight	Light	Heavy	Heavy
Power Consume	Low	High	Limited Fuel
Reliability	High	Low	High

Sensors for attitude determination include low-cost 5-plane coarse sun sensors, magnetometer, gyroscope, and dual-frequency GPS receivers. Apart from this, SNUGLITE has modules for communication and scientific mission execution. In addition, Flight Model (FM) and Engineering Model (EM) were developed separately in SNUGLITE ADCS development stage.

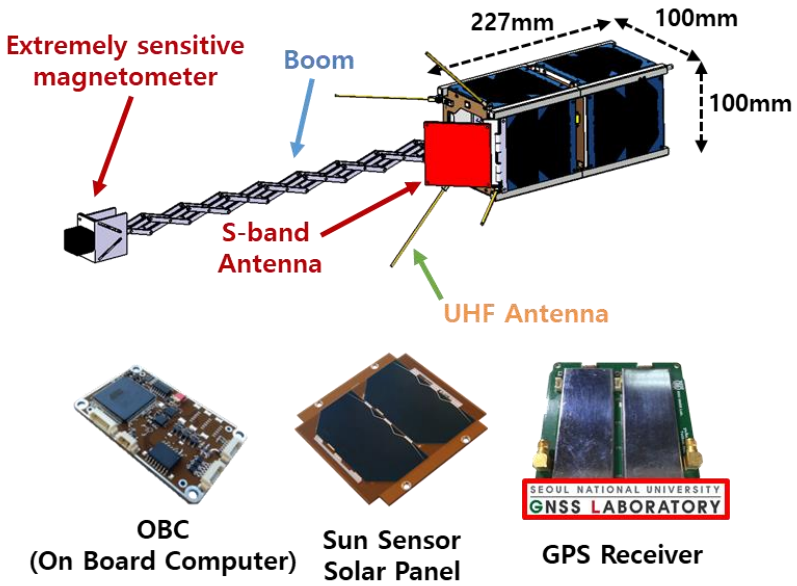

Figure 1.3: SNUGLITE Configuration

The flight model is in actual orbit and includes all payloads for SNUGLITE operation, but the engineering model was developed with minimal configuration to verify ADCS.

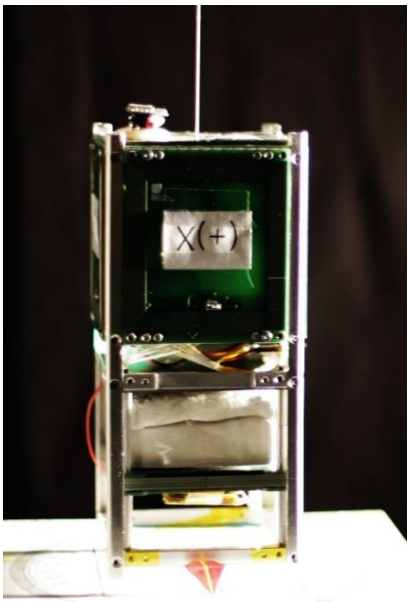

(a) Engineering Model

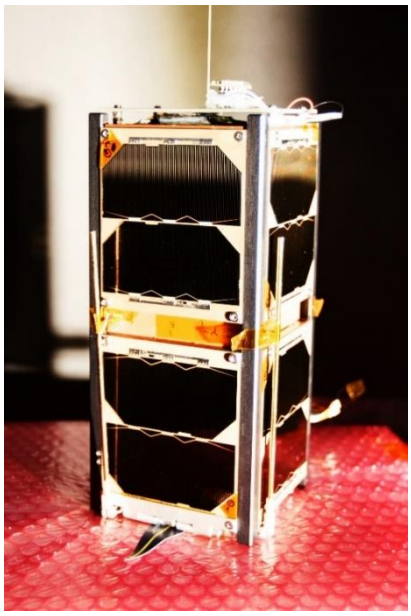

(b) Flight Model

Figure 1.4: SNUGLITE Cube-satellite

Table 1.2: Comparison of EM and FM

Module	Engineering Model	Flight Model
OBC	Gomspace A3200	
Magnetorquer	Self-Developed	Gomspace P110s
Solar Panel	-	
Interstage Panel	Self-Developed	Gomspace GSSB
Communication	Bluetooth	UHF, S-band
Payloads	Dummy Mass	Boom, GPS Receiver*2

As shown in Figure 1.4, FM and EM are basically the same OBCs used for cube satellites [13]. The magnetometer and the gyroscope are in the OBC and use the same sensor for EM and FM. In the case of the magnetorquer, the commercial module was used for the FM, but the EM was equipped with the self-manufactured magnetorquer as PCB based on the same specification of the FM. As communication module, EM has Bluetooth wireless communication for ADCS verification experiment. In contrast, FM is equipped with UHF and s-band module for communication with ground station. Modules not included in the EM include a solar panel, a power management module, a boom and a GPS receiver. In addition, the solar panels, Electrical Power Supply (EPS) system, an extremely sensitive magnetometer at the tip of the boom structure, and GPS receivers are mounted on the FM.

1.1.3. Former Research of SNUGLITE ADCS

In the previous research, from the preliminary design stage to SILS, PILS, and HILS research has been carried out to develop ADCS of SNUGLITE [12]-[14].

In the stage of preliminary design, basic design of ADCS using only magnetorquer was examined. Extended Kalman filter was designed as an attitude determination algorithm. The state variable was

composed of quaternion, angular velocity, and gyro bias. At this time, TRIAD was used as an algorithm to estimate the initial attitude determination. Next, LQR controller was designed as an attitude control algorithm, and the LQG controller combining EKF and LQR controller was designed [12]. Since then, the space environment and SNUGLITE ADCS have been separated and verification through SILS has been studied [14], [15]. And to verify the designed theory, PILS and HILS verification were performed using EM. At this time, the metal compensation method of the magnetometer and the gyroscopes were analyzed because the actual sensor measurement was utilized [16], [17].

1.2. Motivation and Purpose

This thesis is an extension of the earlier work on SNUGLITE ADCS algorithm development and verification. Research is underway to improve ADCS performance with a focus on SNUGLITE FM. In the previous research, SNUGLITE ADCS has been verified by HILS algorithm based on EM. However, as shown in Figure 1.4, FM of SNUGLITE causes problems due to modules that are not installed in EM. The most dominant problem is the magnetic distortion caused by the current. Unlike EM, the magnetometer measurement distortion is

caused by the current flowing through the solar panels. In addition, the current generated by modules cause a control error due to the influence of the geomagnetic field. These problems lead to critical errors in ADCS, so troubleshooting for magnetic field distortion is essential.

Next, it is motivation from the problem of existing HILS verification studies. Magnetorquer, which is an actuator equipped with SNUGLITE, has limitations such as performance limit due to small input torque that depending on the geomagnetic field, and decoupled input control. As a result, there is a difficulty in the ground environment HILS for verifying the performance of ADCS. In particular, existing HILS verification was difficult due to the influence of external torque generated by indoor magnetic field distortion. Distortion of the building magnetic field caused the estimation performance deterioration due to the magnetic noise including the statistical error and the deterioration of the control performance affected by the external magnetic field.

Therefore, this thesis focuses on the verification of the performance of ADCS which is complementary to the existing HILS after first solving the problem of magnetic field distortion which is a problem occurring in FM. First, in case of magnetic field problem, the magnetometer compensation for time-varying bias will be shown and it will be verified by reflecting it in the simulation. And the limit of

existing HILS is supplemented by Helmholtz cage. Using the proposed HILS method, the verification of the performance of ADCS using only the magnetorquer will be presented. Here, the problem of the magnetic field is dominantly induced from the sunlight, so that there is less problem in the building environment. Also, in order to prevent failure of the extremely sensitive magnetometer mounted on the FM due to the magnetic field of the Helmholtz cage, it will be useful as a HILS using EM. In addition, the extremely sensitive magnetometer equipped with FM might be break down due to the magnetic field of the Helmholtz cage larger than the geomagnetic field. Therefore, it will be useful as HILS using EM to protect this sensor. From the experimental results of the previous method and the proposed HILS, the usefulness of the proposed HILS will be shown and the performance of ADCS will be analyzed.

1.3. Literature Survey

As a first part, there is a problem with magnetic field distortion occurring in FM of SNUIGLITE. This can be classified as a problem of measurement distortion related to the estimation and a residual dipole moment problem affecting the control performance. A study on the distortion of measurement has introduced a method of

compensating for cube-satellite, but there is a limitation in estimating it on orbit [18]. A paper solving the problem of measured distortion on the ground have been introduced, but they have not been applied to cube-satellites [19]. For the control performance problem, the residual dipole moment of the cube satellite is introduced. In this regard, there is a study on modeling the dipole moment, but there is a limitation of modeling the residual dipole moment which is already known [20]. In addition, a method of modeling the dipole moment of the space by estimating the dipole moment inside the cube satellite is introduced [21], [22]. But there was also a limitation that this was done only in actual orbit. Differ from existing methods, in this thesis, the problem of magnetic field distortion on the ground is solved. The causes of the magnetic distortion will be modeled as a time-varying bias to compensate for the magnetometer measurement. In addition, the residual dipole moment is modeled for the entire cube-satellite, and the control performance degradation problem will be predicted in orbit using simulation.

Second, the limitations of previous HILS research methods are introduced. HILS studies of cube-satellite ADCS have been studied in order to stabilize angular velocity, passive control method based on geomagnetic field alignment, and method of maintaining nadir-pointing using reaction wheels. These HILS verification of ADCS have been conducted using Helmholtz cage (or Helmholtz coil). The

existing HILS using Helmholtz cage is divided into two types. The first is the use of Helmholtz cage to verify the angular velocity stabilization and the passive control method. In this case, after fixing the magnetic field vector generated by Helmholtz cage, it is the most commonly used method of performing HILS to determine whether a cube-satellite attenuates angular velocity or aligns magnetic field vectors well [23]. HILS, which combines air bearing and Helmholtz cage, has been studied as a HILS for verifying the nadir-pointing control. In this studies, Helmholtz cage was used for the attitude determination by simulating the magnetic field vector using the geomagnetic field model on the orbit [24]-[26]. However, there is a limit to the above documents that it is not suitable for the nadir-pointing ADCS with only magnetorquer. Therefore, a complementary HILS method is needed to solve this problem.

1.4. Outline of Research

This thesis is largely composed of three parts. The first is the introduction of cube-satellite ADCS algorithm, the second is the method of solving the magnetic field distortion and verifying it by simulation, and the third is the HILS verification of ADCS using Helmholtz cage to complement the limit of existing HILS.

First, the algorithm introduction part introduces the basic coordinate system used in ADCS, and then the equation of motion for the cube-satellite on the orbit is modeled. In addition, Extended Kalman filter is constructed to estimate the attitude of a cube-satellite by fusing given sun sensors, magnetometer, and gyroscope measurements. LQR controller is designed to maintain the nadir-pointing by constructing a cost function for a given linear system and input and calculating the optimal solution.

In the second part, the problem of magnetic field distortion is divided into attitude determination problem and attitude control problem. The problem of measurement distortion, which is an attitude determination problem, is defined as a current compensation, a temperature compensation, and a metal compensation of a magnetic field sensor. In the case of the residual dipole moment problem, which is the attitude control problem, the disturbance is predicted and reflected in the process noise of extended Kalman filter.

Finally, it is a part of HILS verification of ADCS using Helmholtz cage. In this section, Helmholtz cage for HILS is designed and fabricated. And the performance of SNUGITE ADCS is verified by HILS verification using it.

1.5. Contribution

The contributions presented in this thesis are divided into two parts: the algorithm for the magnetic field distortion and HILS verification using the Helmholtz cage.

First, an ADCS algorithm is developed that reflects the magnetic field measurement compensation and the residual control error as part of the magnetic field distortion of the cube-satellite. The error of the magnetic field vector, which is an important indicator of direction in low orbit cube satellites, causes serious errors in ADCS. As a solution to this problem, the magnetic field measurement problem of the cube-satellite is resolved by estimating and compensating the magnetic field measurement error factors on the ground, unlike the conventional method of estimating this on the orbit. Also, the performance of ADCS in the space environment is predicted by modeling the disturbance of residual dipole moment.

Next, HILS verification using Helmholtz cage is performed as a complement to the previous HILS methods. The accuracy of the HILS verification is demonstrated by introducing the Helmholtz cage as a limitation of the previous HILS verification. This problem is solved by controlling the magnetic field vector generated from the Helmholtz cage. That is, the degradation of the estimation performance due to the magnetic field including the statistical error characteristic in the

ground environment and the deterioration of the control performance due to the small input torque of the magnetorquer vulnerable to the disturbance are solved. In order to verify the usefulness of the proposed method, a single-axis ADCS HILS verification of SNUGLITE cube-satellite is presented. The proposed method can verify ADCS to maintain the nadir-pointing contol by using only the magnetorquer in the ground environment.

Chapter 2

Algorithm of

Attitude Determination and Control System

In this chapter, the ADCS algorithm of SNUGLITE cube-satellite is introduced. Theoretical background is described for ADCS according to SNUGLITE operational scenario. First, the overall system configuration is introduced and the coordinate system used in SNUGLITE is defined. Then, the angular rate attenuation control for initial angular velocity stabilization is introduced. The angular velocity attenuation control is performed by B-dot control using the rate change of the magnetic field measurement value. When the angular velocity is stabilized, an algorithm for maintaining the nadir-pointing is performed. Extended Kalman filter and Linear Quadratic Regulator (LQR) controller are designed, and the theoretical backgrounds are introduced.

2.1. Overall System Configuration

The entire system of SNUGLITE ADCS is configured as shown in Figure 2.1 below.

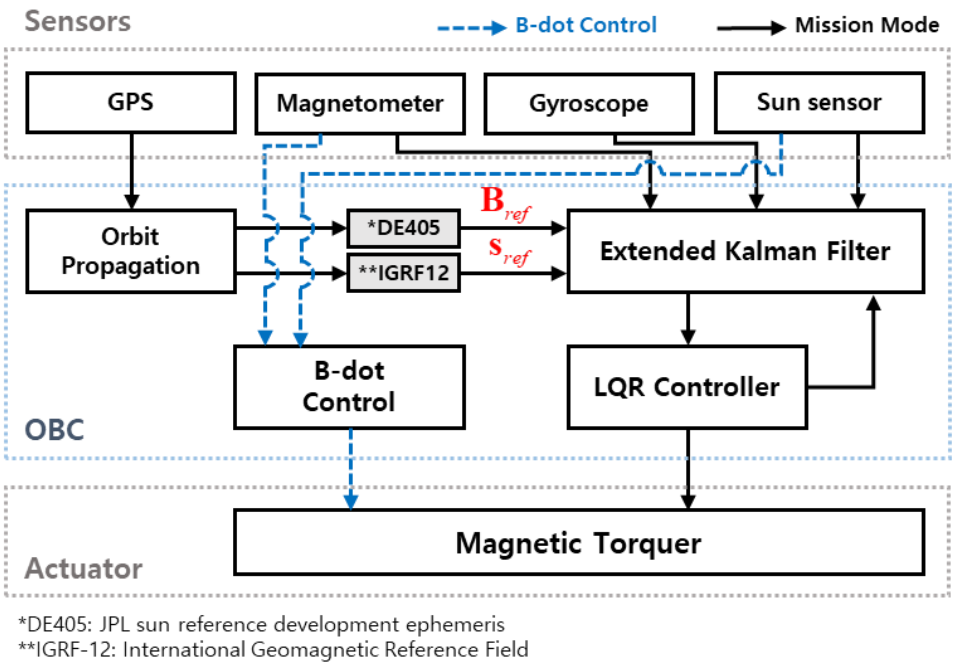

Figure 2.1: Overall System of SNUGLITE ADCS

The parts that constitute ADCS are divided into sensors, On-Board-Computer (OBC), and actuator. And two modes for operation. The first is the B-dot control mode for angular velocity attenuation, and the second is the mission mode for scientific mission execution.

In the B-dot control mode, a controller is designed to reduce the

rate change of magnetic measurement using the magnetic sensor and the sun sensor. Here, the role of the sun sensor is used for detecting the eclipse. This is because the magnetic field measurement is distorted by sunlight. It will be explained in detail in the next chapter. Therefore, the B-dot control mode is performed during the eclipse period, and when converging within a certain angular velocity, the mode is switched to the mission mode.

In the mission mode, attitude determination and control are performed using all sensors. This is the goal of the nadir-pointing control to carry out the scientific missions. GPS measurements provide a position on the orbit, which is used to calculate the reference vector from the magnetic field model (IGRF-12) and the solar system model (DE405). Using the reference vectors, EKF is constructed using the measurements of magnetometer, gyroscope and sun sensors. Then, the estimated state from EKF are provided to LQR controller and used for attitude control. And the control input calculated by LQR controller is reflected in the dynamics of EKF.

2.2. Coordinate System

In order to express the attitude of SNUGLITE by the equation of motion, the following coordinate system is used.

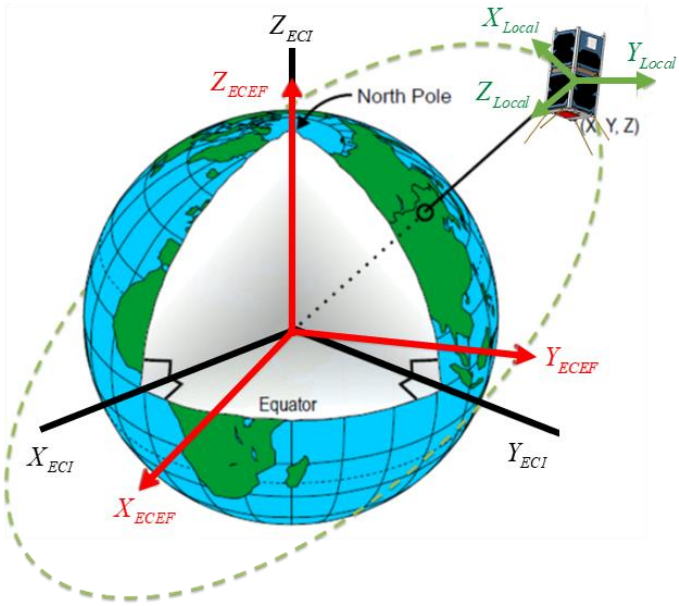

Figure 2.2: Coordinate System of

ECI, ECEF, Local Frame

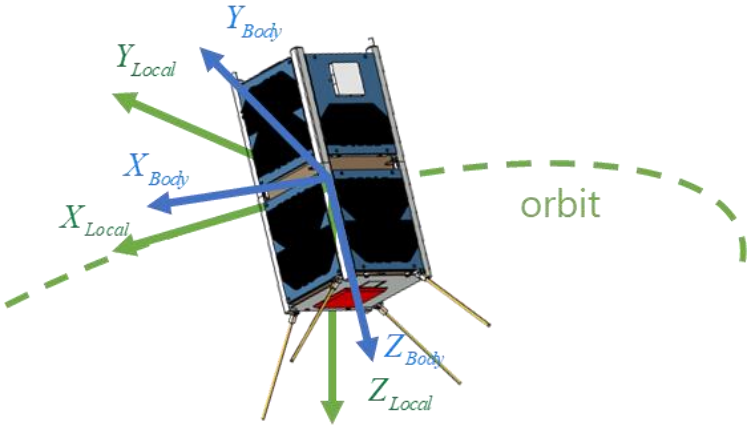

Figure 2.3: Coordinate System of

Body, Local Frame

2.2.1. Earth-Centered Inertial (ECI) Frame

Basically, an inertial frame is defined as a reference frame in which Newton's laws of motion are valid. All inertial sensors produce measurements from a defined inertial coordinate system. However, satellite coordinates and velocity need to be expressed around the earth. Therefore, the ECI coordinate system was introduced as a coordinate system for representing the environment around the earth. Earth rotation is not considered. This coordinate system is defined as follows [27], [28].

1) The origin of ECI frame is at the center of mass of the Earth.
2) The x−axis is in the equatorial plane pointing towards the vernal equinox.
3) The z−axis is along axis of the Earth's rotation. Theoretically, this axis is fixed, but in fact it is affected by earth rotation, moon and earth interference, precession, and nutation.
4) The y−axis is the direction according to the right−hand rule of the x and the z axes.

2.2.2. Earth-Centered Earth-Fixed (ECEF) Frame

This coordinate system is similar to the ECI coordinate system. Because it shares the same origin with the z−axis. Unlike the ECI, this coordinate system considers the earth's rotation. Therefore, the

x and y axes differ from the ECI coordinate system by the angle of the earth rotation. This coordinate system is defined as follows [27], [28].

1) The origin of ECEF frame is at the center of mass of the Earth.
2) The x-axis in the equatorial plane directed through the Greenwich Meridian.
3) The z-axis is along axis of the Earth's rotation. It same as ECI.
4) The y-axis is the direction according to the right-hand rule of the x and the z axes.

2.2.3. Local Frame

The exact name of local frame is Locally-Horizontal-Vertical (LHV) frame, but in this thesis, it is defined as local frame. This coordinate system is based on the cube-satellite orbit. Therefore, it can be said to be a coordinate system which changes continuously according to the position on the orbit. This coordinate system is defined as follows [12].

1) The origin of local frame is at the center of gravity of the cube-satellite.
2) The x-axis is the direction of translational motion and is the same direction as the velocity vector on the orbit.

3) The z-axis is the direction of the center of the earth.

4) The y-axis is the direction according to the right-hand rule of the x and the z axes.

In ECI coordinate system, local frame changes a continuous circular motion with respect to the center of the earth. The relationship between the ECI coordinate system and local coordinate system is expressed by the angular velocity according to the circular motion. It is called mean motion, and is defined as follows.

$$mR_e n^2 = m\frac{GM}{R^2} = mg \tag{2.1}$$

$$n \triangleq \sqrt{\frac{g}{R}} \tag{2.2}$$

here, the orbit of the cube-satellite is assumed to be a circular orbit with a small eccentricity.

2.2.4. Body Frame

As the most well-known coordinate system, Body frame is a coordinate system fixed to the cube-satellite. In this paper, it is assumed that body frame coincides with sensor frame. This coordinate system is defined as follows [12].

1) The origin of local frame is at the center of gravity of the cube-satellite.

2) The x-axis is defined as the direction perpendicular to the side of the cube-satellite.
3) The y-axis is defined as the direction perpendicular to another side of the cube-satellite. It is clockwise rotated 90 degrees from the x-axis.
4) The z-axis is the direction according to the right-hand rule of the x and the y axes.

The body angular velocity (p, q, r) of the cube-satellite is defined from the relationship between the ECI and body frames. Euler angles (ϕ, θ, ψ) are also defined from the relationship of the body frame from the local coordinate system. Now, the relationship between coordinate systems will be expressed.

2.3. Coordinate Transformations

In order to mathematically represent the motion of the cube-satellite, a transformation relation between the coordinate systems defined above is required. Through the transformation matrix between each coordinate system, motion of equations expressed in another coordinate system can be unified into one coordinate system.

2.3.1. Transformation Between ECEF and ECI Frame

The ECI and ECEF coordinate systems are coordinate systems that share the z−axis. Therefore, considering the rotation of the earth about the z−axis from the ECI coordinate system, it can be converted to the ECEF coordinate system.

$$R_{ECI}^{ECEF} = \begin{bmatrix} \cos\Omega_e t & \sin\Omega_e t & 0 \\ -\sin\Omega_e t & \cos\Omega_e t & 0 \\ 0 & 0 & 1 \end{bmatrix} \tag{2.3}$$

$$R_{ECI}^{ECEF} = \left(R_{ECEF}^{ECI}\right)^{-1} = \left(R_{ECEF}^{ECI}\right)^{T} \tag{2.4}$$

The criterion for earth rotation is calculated by Greenwich Mean Sidereal Time. And, in this thesis, nutation and polar motion are neglected for computational efficiency.

2.3.2. Transformation Between ECI and Local Frame

From the position and the velocity of the cube−satellite, the relationship between ECI and local coordinate system is defined. The position and the velocity can be known by the GPS measurement, which is expressed by the ECEF coordinate system. Therefore, when a given measurement is converted into an ECI coordinate system, it can be written as follows.

$$r_{ECI} = R_{ECEF}^{ECI} r_{ECEF} \tag{2.5}$$

$$v_{ECI} = R_{ECEF}^{ECI} v_{ECEF} \tag{2.6}$$

Assuming that the orbit is an ellipse, the relationship between ECI and local coordinate system can be obtained by using the Radial-In track-Cross track (RIC) frame [13].

$$\hat{R} = \frac{r_{ECI}}{|r_{ECI}|} \tag{2.7}$$

$$\hat{C} = \frac{r_{ECI} \times v_{ECI}}{|r_{ECI} \times v_{ECI}|} \tag{2.8}$$

$$\hat{I} = \hat{C} \times \hat{R} \tag{2.9}$$

A coordinate transformation matrix is defined by combining the three vectors of the above equations 2.7 to 2.9.

$$R_{Local}^{ECI} = \begin{bmatrix} \hat{I} & -\hat{C} & -\hat{R} \end{bmatrix} \tag{2.10}$$

$$R_{ECI}^{Local} = \left(R_{Local}^{ECI}\right)^{-1} = \left(R_{Local}^{ECI}\right)^{T} \tag{2.11}$$

2.3.3. Transformation Between Local and Body Frame

The relationship between local and body coordinate system can be represented by Euler angle rotations composed of 3-2-1 transformation [12], [29].

$$R_{Local}^{Body} = R(\phi,1)\cdot R(\theta,2)\cdot R(\psi,3) \tag{2.12}$$

here,

$$R(\phi,1) = \begin{bmatrix} 1 & 0 & 0 \\ 0 & \cos\phi & \sin\phi \\ 0 & -\sin\phi & \cos\phi \end{bmatrix}$$

$$R(\theta,2) = \begin{bmatrix} \cos\theta & 0 & \sin\theta \\ 0 & 1 & 0 \\ -\sin\theta & 0 & \cos\theta \end{bmatrix}$$

$$R(\psi,3) = \begin{bmatrix} \cos\psi & \sin\psi & 0 \\ -\sin\psi & \cos\psi & 0 \\ 0 & 0 & 1 \end{bmatrix}$$

However, since the motion of the cube-satellite on the orbit may cause singularity, a quaternion is used to express the attitude to prevent this. Therefore, the transformation matrix can be expressed as a quaternion as follow.

$$R_{Local}^{Body} = \begin{bmatrix} q_0^2+q_1^2-q_2^2-q_3^2 & 2(q_1q_2+q_0q_3) & 2(q_1q_3-q_0q_2) \\ 2(q_1q_2-q_0q_3) & q_0^2-q_1^2+q_2^2-q_3^2 & 2(q_2q_3+q_0q_1) \\ 2(q_1q_3+q_0q_2) & 2(q_2q_3-q_0q_1) & q_0^2-q_1^2-q_2^2+q_3^2 \end{bmatrix} \tag{2.13}$$

2.4. Dynamics Modeling

To represent the cube-satellite attitude as an equation of motion, assume the cube-satellite as a rigid body. And, it is assumed that the body frame is fixed to the center of mass. The derivation of detailed equations is described in the book of Bryson [29]. And the derived equation includes the work of Kim et al [12].

2.4.1. Nonlinear Equations of Motion

The moment for the rotational motion of the rigid body can be written as in Eq. 2.14.

$$M = H_I = H_B + \Omega \times H \tag{2.14}$$

here,

$$\Omega = \begin{bmatrix} p \\ q \\ r \end{bmatrix},\ \bar{\bar{I}} = \begin{bmatrix} I_x & I_{xy} & I_{xz} \\ I_{yx} & I_y & I_{yz} \\ I_{zx} & I_{zy} & I_z \end{bmatrix},\ H = \bar{\bar{I}} \cdot \Omega = \begin{bmatrix} I_x p + I_{xy} q + I_{xz} r \\ I_{yx} p + I_y q + I_{yz} r \\ I_{zx} p + I_{zy} q + I_z r \end{bmatrix}$$

Equation 2.14 can be rewritten as follows.

$$\begin{bmatrix} M_x \\ M_y \\ M_z \end{bmatrix} = \begin{bmatrix} I_x \dot{p} + (I_z - I_y) qr + I_{xy}(\dot{q} - pr) + I_{xz}(\dot{r} + pq) + I_{xz}(q^2 - r^2) \\ I_y \dot{q} + (I_x - I_z) rp + I_{yz}(\dot{r} - pq) + I_{yz}(\dot{p} + qr) + I_{zx}(r^2 - p^2) \\ I_z \dot{r} + (I_y - I_x) pq + I_{zx}(\dot{p} - qr) + I_{zy}(\dot{q} + rp) + I_{xy}(p^2 - q^2) \end{bmatrix} \tag{2.15}$$

Since the cube-satellite is a rigid body and the center of gravity is assumed to be located at the center of the rectangular parallelepiped, the diagonal component of the moment of inertia becomes zero.

$$\bar{\bar{I}} = \begin{bmatrix} I_x & 0 & 0 \\ 0 & I_y & 0 \\ 0 & 0 & I_z \end{bmatrix}, \ (I_{xy} = I_{zx} = I_{yz} = 0) \tag{2.16}$$

Therefore, the Euler equations are derived.

$$\begin{bmatrix} M_x \\ M_y \\ M_z \end{bmatrix} = \begin{bmatrix} I_x \dot{p} + (I_z - I_y) qr \\ I_y \dot{q} + (I_x - I_z) rp \\ I_z \dot{r} + (I_y - I_x) pq \end{bmatrix} \tag{2.17}$$

The body-fixed angular velocity (p, q, r) can be represented by Euler angles using 3-2-1 transformation. Here, the mean motion is considered.

$$\begin{bmatrix} p \\ q \\ r \end{bmatrix} = \begin{bmatrix} 1 & 0 & -\sin\theta \\ 0 & \cos\phi & \cos\theta\sin\phi \\ 0 & -\sin\phi & \cos\theta\cos\phi \end{bmatrix} \begin{bmatrix} \dot{\phi} \\ \dot{\theta} \\ \dot{\psi} \end{bmatrix} - \begin{bmatrix} \sin\psi\cos\theta \\ \sin\psi\sin\theta\sin\phi + \cos\psi\cos\phi \\ \sin\psi\sin\theta\cos\phi - \cos\psi\sin\phi \end{bmatrix} n \tag{2.18}$$

Equation 2.18 can be rewritten as rate change of Euler angles as follows.

$$
\begin{bmatrix} \dot{\phi} \\ \dot{\theta} \\ \dot{\psi} \end{bmatrix} = \begin{bmatrix} 1 & \tan\theta\sin\phi & \tan\theta\cos\phi \\ 0 & \cos\phi & -\sin\phi \\ 0 & \sec\theta\sin\phi & \sec\theta\cos\phi \end{bmatrix} \begin{bmatrix} p \\ q \\ r \end{bmatrix}
$$

$$
+ \begin{bmatrix} 1 & \tan\theta\sin\phi & \tan\theta\cos\phi \\ 0 & \cos\phi & -\sin\phi \\ 0 & \sec\theta\sin\phi & \sec\theta\cos\phi \end{bmatrix} \begin{bmatrix} \sin\psi\cos\theta \\ \sin\psi\sin\theta\sin\phi + \cos\psi\cos\phi \\ \sin\psi\sin\theta\cos\phi - \cos\psi\sin\phi \end{bmatrix} n \tag{2.19}
$$

The external moments considered in this thesis are only the gravity gradient torque and the magnetic input torque. Since gravity gradient torque is the most dominant torque on the orbit, solar radiation pressure, and air friction are considered in the simulation. The gravity gradient torque is defined as follows:

$$
\begin{aligned}
\tau_{gg} &= \frac{3\mu_e}{r_c^3} \hat{r}_c \times (I \cdot \hat{r}_c) \\
&= 3n^2 \begin{bmatrix} (I_z - I_y)\sin\phi\cos\phi\left(\cos\theta\right)^2 \\ (I_z - I_x)\sin\theta\cos\theta\cos\phi \\ (I_x - I_y)\sin\phi\sin\theta\cos\theta \end{bmatrix}
\end{aligned} \tag{2.20}
$$

here, $\hat{r}_c$ is a unit vector representing the direction from the center of the earth to the center of gravity of the cube-satellite.

The torque generated by the magnetorquer mounted on the cube-satellite appears as a cross product of the input dipole moment and the geomagnetic field.

$$
\begin{aligned}
\tau_{mt} &= \boldsymbol{\mu} \times \mathbf{B} \\
&= \begin{bmatrix} \mu_y B_z - \mu_z B_y \\ \mu_z B_x - \mu_x B_z \\ \mu_x B_y - \mu_y B_x \end{bmatrix}
\end{aligned} \tag{2.21}
$$

From the Euler equations derived from Eq. 2.17, the nonlinear equations of motion are derived by taking into account the considered gravity gradient torque and input torque.

$$
\begin{aligned}
\begin{bmatrix} M_x \\ M_y \\ M_z \end{bmatrix} &= \begin{bmatrix} I_x \dot{p} + (I_z - I_y) qr \\ I_y \dot{q} + (I_x - I_z) rp \\ I_z \dot{r} + (I_y - I_x) pq \end{bmatrix} \\
&= 3n^2 \begin{bmatrix} (I_z - I_y) \sin\phi \cos\phi \left(\cos\theta\right)^2 \\ (I_z - I_x) \sin\theta \cos\theta \cos\phi \\ (I_x - I_y) \sin\phi \sin\theta \cos\theta \end{bmatrix} + \begin{bmatrix} \mu_y B_z - \mu_z B_y \\ \mu_z B_x - \mu_x B_z \\ \mu_x B_y - \mu_y B_x \end{bmatrix}
\end{aligned} \tag{2.22}
$$

It can be written for the rate of change of body-fixed angular velocity.

$$
\begin{aligned}
\dot{p} &= -\frac{I_z - I_y}{I_x} qr + \frac{3n^2 (I_z - I_y)}{I_x} \sin\phi \cos\phi \left(\cos\theta\right)^2 + \frac{1}{I_x}\left(\mu_y B_z - \mu_z B_y\right) \\
\dot{q} &= -\frac{I_x - I_z}{I_y} rp + \frac{3n^2 (I_z - I_x)}{I_y} \sin\theta \cos\theta \cos\phi + \frac{1}{I_y}\left(\mu_z B_x - \mu_x B_z\right) \\
\dot{r} &= -\frac{I_y - I_x}{I_z} pq + \frac{3n^2 (I_x - I_y)}{I_z} \sin\phi \sin\theta \cos\theta + \frac{1}{I_z}\left(\mu_x B_y - \mu_y B_x\right)
\end{aligned} \tag{2.23}
$$

The derived nonlinear equation is used for time propagation in the simulation.

2.4.2. Linearized Equations of Motion

If the cube satellite is stabilized at the initial angular velocity, the attitude will change in an insufficient range. Therefore, a small angle approximation is used to linearize the derived nonlinear equations, and the following two conditions are assumed.

1) Small angle approximation: $\phi, \theta, \psi << 1$

2) Small angular rate change for pitch and yaw: $\dot{\psi}, \dot{\theta} \ll n$

Using the above conditions, equations 2.18 and 2.19 are linearized as follows.

$$\begin{bmatrix} p \\ q \\ r \end{bmatrix} \approx \begin{bmatrix} \dot{\phi} - \dot{\psi}\theta - n\psi \\ \dot{\theta} + \dot{\psi}\phi - n \\ \dot{\psi} - \dot{\theta}\phi + n\phi \end{bmatrix} \tag{2.24}$$

$$\begin{bmatrix} \dot{\phi} \\ \dot{\theta} \\ \dot{\psi} \end{bmatrix} \approx \begin{bmatrix} p + n\psi \\ q + n \\ r - n\phi \end{bmatrix} \tag{2.25}$$

The product of angular velocities is approximated when equations 2.24 and 2.25 are applied.

$$\begin{aligned} qr &= \left(\dot{\theta} - n\right)\left(\dot{\psi} + n\phi\right) \approx -nr \\ rp &= \left(\dot{\psi} + n\phi\right)\left(\dot{\phi} - n\psi\right) \approx 0 \\ pq &= \left(\dot{\phi} - n\psi\right)\left(\dot{\theta} - n\right) \approx -np \end{aligned} \tag{2.26}$$

Thus, the linearized dynamics of the cube-satellite can be expressed as:

$$
\begin{aligned}
\dot{p} &\approx \frac{n(I_z - I_y)}{I_x} r + \frac{3n^2(I_z - I_y)}{I_x} \phi + \frac{1}{I_x}\left(\mu_y B_z - \mu_z B_y\right) \\
\dot{q} &\approx \frac{3n^2(I_z - I_x)}{I_y} \theta + \frac{1}{I_y}\left(\mu_z B_x - \mu_x B_z\right) \\
\dot{r} &\approx \frac{n(I_y - I_x)}{I_z} p + \frac{1}{I_z}\left(\mu_x B_y - \mu_y B_x\right)
\end{aligned}
\tag{2.27}
$$

2.5. Angular Velocity Attenuation for Initial Phase

In the angular velocity attenuation mode, it is necessary to reduce the angular velocity of the cube-satellite as much as possible to facilitate the smooth functioning of the nadir-pointing control. The reason is that Equation 2.27 used in the algorithm assumes highly small angle. However, the gyroscope equipped for the angular velocity measurement cannot be used because of the presence of the bias. To solve this problem, a magnetometer is utilized in the angular velocity attenuation mode. This is called B-dot control. The method consists of a simple algorithm that can be performed by calculating the rate of change of the magnetic field measurements [12].

$$u = -K_{bdot} \cdot \frac{B_k - B_{k-1}}{\Delta t},\ K_{bdot} > 0 \tag{2.28}$$

Thereafter, when the angular rate is converged into a predetermined value, the angular velocity attenuation mode is switched to the mission mode. This algorithm is also performed only during the eclipse period. The reason is for the stability of the angular velocity attenuation because the magnetic field measurement value is distorted in the sun period. Therefore, it is judged whether B−dot control is performed by discriminating the eclipse period from the sun sensors. Problems with magnetic field distortion will be discussed in detail in the next chapter.

2.6. Attitude Determination Algorithm

In this section, the theoretical background of the attitude determination algorithm is described. The attitude determination algorithm consists of TRIAD method and extended Kalman filter. TRIAD method is an initial attitude determination algorithm, which has the merit that there is an error but it is simple. Extended Kalman Filter is a widely used algorithm in the attitude estimation algorithm, the nonlinear system is linearized to form Kalman filter.

2.6.1. TRIAD Method

TRIAD algorithm uses two vectors to determine the initial attitude of the cube-satellite. In this thesis, magnetic field vector and sun vector are applied to TRIAD algorithm. A vector is constructed using magnetometer measurement and sun sensor measurements and compared with a vector constructed using a magnetic field model and a solar system model [14], [15], [30].

$$\begin{cases} \mathbf{t}_x^{Body} = \mathbf{s}_{meas} \\ \mathbf{t}_y^{Body} = \dfrac{\mathbf{s}_{meas} \times \mathbf{B}_{meas}}{|\mathbf{s}_{meas} \times \mathbf{B}_{meas}|} \\ \mathbf{t}_z^{Body} = \dfrac{\mathbf{t}_x^{Body} \times \mathbf{t}_y^{Body}}{|\mathbf{t}_x^{Body} \times \mathbf{t}_y^{Body}|} \end{cases}, \quad \begin{cases} \mathbf{t}_x^{Local} = \mathbf{s}_{\text{model}} \\ \mathbf{t}_y^{Local} = \dfrac{\mathbf{s}_{\text{model}} \times \mathbf{B}_{\text{model}}}{|\mathbf{s}_{\text{model}} \times \mathbf{B}_{\text{model}}|} \\ \mathbf{t}_z^{Local} = \dfrac{\mathbf{t}_x^{\text{model}} \times \mathbf{t}_y^{\text{model}}}{|\mathbf{t}_x^{\text{model}} \times \mathbf{t}_y^{\text{model}}|} \end{cases} \tag{2.29}$$

Combining the two vectors constitutes a Direction Cosine Matrix (DCM).

$$R_{TRIAD}^{Body} = \begin{bmatrix} \mathbf{t}_x^{Body} & \mathbf{t}_y^{Body} & \mathbf{t}_z^{Body} \end{bmatrix}, \; R_{TRIAD}^{Local} = \begin{bmatrix} \mathbf{t}_x^{Local} & \mathbf{t}_y^{Local} & \mathbf{t}_z^{Local} \end{bmatrix} \tag{2.30}$$

$$R_{TRIAD} = R_{TRIAD}^{Body} \left(R_{TRIAD}^{Local} \right)^T \tag{2.31}$$

Since DCM is the coordinate transformation matrix of Eq. 2.13, it is easy to calculate the initial quaternion $(\mathbf{q}_0)$.

2.6.2. Extended Kalman Filter

The derivation process of the attitude estimation algorithm includes the previous works [12]–[14], [31]. The states of extended Kalman filter consist of quaternion, angular velocity, and gyro bias.

$$\mathbf{x}(t)=\begin{bmatrix}\mathbf{q}(t)\\ \boldsymbol{\omega}(t)\\ \mathbf{b}(t)\end{bmatrix}_{10\times 1}, \quad \begin{aligned}\mathbf{q}&=\begin{bmatrix}q_0 & q_1 & q_2 & q_3\end{bmatrix}^T\\ \boldsymbol{\omega}&=\begin{bmatrix}\omega_x & \omega_y & \omega_z\end{bmatrix}^T\\ \mathbf{b}&=\begin{bmatrix}b_x & b_y & b_z\end{bmatrix}^T\end{aligned} \tag{2.32}$$

To obtain the nonlinear system equation of EKF, an equation of each state variable is derived. First, the state equation for the quaternion is derived as follows [12].

$$\dot{\mathbf{q}}=\frac{1}{2}\boldsymbol{\Omega}(\boldsymbol{\omega})\mathbf{q}=\frac{1}{2}\boldsymbol{\Xi}(\mathbf{q})\boldsymbol{\omega} \tag{2.33}$$

here,

$$\boldsymbol{\Omega}(\boldsymbol{\omega})=\begin{bmatrix}0 & -\omega_x & -\omega_y & -\omega_z\\ \omega_x & 0 & \omega_z & -\omega_y\\ \omega_y & -\omega_z & 0 & \omega_x\\ \omega_z & \omega_y & -\omega_x & 0\end{bmatrix}_{4\times 4}, \quad \boldsymbol{\Xi}(\mathbf{q})=\begin{bmatrix}-q_1 & -q_2 & -q_3\\ q_0 & -q_3 & q_2\\ q_3 & q_0 & -q_1\\ -q_2 & q_1 & q_0\end{bmatrix}_{4\times 3}$$

Next, the state equation for the angular velocity is derived from Equation 2.14.

$$\dot{\boldsymbol{\omega}}=\bar{\bar{I}}^{-1}\left(\boldsymbol{\mu}\times\mathbf{B}-\boldsymbol{\omega}\times(\bar{\bar{I}}\cdot\boldsymbol{\omega})\right) \tag{2.34}$$

Gyro bias is modeled as a random work. Therefore, the state equation consists of a zero matrix. This is because there is a large temperature variation in space with sun existence, and the gyro bias is easily affected by temperature.

$$\dot{\mathbf{b}} = \mathbf{0}_{3\times3} \tag{2.35}$$

The nonlinear system equation of EKF is obtained by reflecting the modeling error of each state variable equations derived from Equation 2.33~35 as the process noise. Here, the process noise $\mathbf{w}(t)$ is assumed to be zero−mean white noise with variance matrix Q.

$$\frac{d}{dt}\mathbf{x}(t) = f\left(\mathbf{x}(t), \boldsymbol{\mu}(t)\right) + \mathbf{w}(t), \quad \mathbf{w}(t) \sim N(0, Q) \tag{2.36}$$

$$\begin{bmatrix} \dot{\mathbf{q}}(t) \\ \dot{\boldsymbol{\omega}}(t) \\ \dot{\mathbf{b}}(t) \end{bmatrix} + \mathbf{w}(t) = \begin{bmatrix} \frac{1}{2}\boldsymbol{\Omega}(\boldsymbol{\omega}_{LB}^{B})\mathbf{q} \\ \overline{\overline{I}}^{-1}\left(\boldsymbol{\mu}\times\mathbf{B} - \boldsymbol{\omega}\times(\overline{\overline{I}}\cdot\boldsymbol{\omega})\right) \\ \mathbf{0}_{3\times3} \end{bmatrix} + \begin{bmatrix} \mathbf{0} \\ \boldsymbol{\eta}_{drift} \\ \boldsymbol{\eta}_{bias} \end{bmatrix} \tag{2.37}$$

$\boldsymbol{\omega}_{LB}^{B}$ in the quaternion term means the angular velocity defined in the body frame. It means that vector rotation from local to body frame. However, since gyro measurements do not provide $\boldsymbol{\omega}_{LB}^{B}$, it is necessary to express the measurement in accordance with the coordinate system. To do this, the body fixed angular velocity p, q, r is defined as the angular velocity from the ECI to the body coordinate

system $\boldsymbol{\omega}_{EB}^{B} = \begin{bmatrix} p & q & r \end{bmatrix}^{T}$. Using the relationship between each coordinate system, the body-fixed angular velocity can be expressed as:

$$\begin{aligned} \boldsymbol{\omega}_{EB}^{B} &= \boldsymbol{\omega}_{EL}^{B} + \boldsymbol{\omega}_{LB}^{B} \\ &= \boldsymbol{\omega}_{LB}^{B} + R_{Local}^{Body} \boldsymbol{\omega}_{EL}^{L} \\ &= \boldsymbol{\omega}_{LB}^{B} + R_{Local}^{Body} \begin{bmatrix} 0 \\ -n \\ 0 \end{bmatrix} \end{aligned} \tag{2.38}$$

Thus, each component of the angular velocity measurement is defined. Since the noise of angular velocity is included in the measurement noise, it is not considered in the system equation.

$$\boldsymbol{\omega}_{meas} = \boldsymbol{\omega}_{EB}^{B} + \mathbf{b} \tag{2.39}$$

The covariance matrix Q reflects disturbances that are not modeled in dynamic equations as noise.

$$Q = \begin{bmatrix} \mathbf{0} & \mathbf{0} & \mathbf{0} \\ \mathbf{0} & (\sigma_{gg}^{2} + \sigma_{sr}^{2} + \sigma_{ad}^{2} + \sigma_{mdt}^{2}) I_{3\times3} & \mathbf{0} \\ \mathbf{0} & \mathbf{0} & (\sigma_{rrw}^{2}) I_{3\times3} \end{bmatrix} \tag{2.40}$$

here, the calculation of the disturbance component of the process noise will be explained in the next chapter.

The measurement vector consists of magnetometer, sun sensor, and gyroscope measurements.

$$\mathbf{z}(t) = \begin{bmatrix} \mathbf{B}_{meas} \\ \mathbf{s}_{meas} \\ \boldsymbol{\omega}_{meas} \end{bmatrix} \tag{2.41}$$

The nonlinear measurement equation can be composed of a magnetic field model, a solar system model, and an estimated angular velocity and bias. The values calculated from the model are transformed into body frames through the respective coordinate transformations.

$$h(\mathbf{x}(t)) = \begin{bmatrix} \mathbf{B} \\ \mathbf{s} \\ \boldsymbol{\omega} + \mathbf{b} \end{bmatrix} = \begin{bmatrix} R_{Local}^{Body} R_{ECI}^{Local} R_{ECEF}^{ECI} R_{NED}^{ECEF} \dfrac{\mathbf{B}_{IGRF}}{|\mathbf{B}_{IGRF}|} \\ R_{Local}^{Body} R_{ECI}^{Local} \mathbf{s}_{DE\,405} \\ \boldsymbol{\omega} + \mathbf{b} \end{bmatrix} \tag{2.42}$$

The innovation vector can be constructed by the difference between the measurement and the nonlinear measurement equation.

$$\mathbf{y}(t) = \mathbf{z}(t) - h(\mathbf{x}(t)) \tag{2.43}$$

Now linearizing the equation given by the definition of extended Kalman filter leads to equation 2.44 [31]. Where $\mathbf{u}$ is an input matrix and is equal to $\boldsymbol{\mu}$. Here, the determination of the measurement noise will be explained in the next chapter.

$$\begin{aligned} \dot{\mathbf{x}} &= F\mathbf{x} + G\mathbf{u} + \Gamma\mathbf{w} \\ \mathbf{z} &= H\mathbf{x} + \mathbf{v} \end{aligned}, \quad \begin{aligned} \mathbf{w} &\sim N(0, Q) \\ \mathbf{v} &\sim N(0, R) \end{aligned} \tag{2.44}$$

The transition matrix F is linearized through a small angle approximation in the same way as in Section 2.4.2.

$$F = \frac{\partial f}{\partial \mathbf{x}} = \begin{bmatrix} \frac{\partial \dot{\mathbf{q}}}{\partial \mathbf{q}} & \frac{\partial \dot{\mathbf{q}}}{\partial \boldsymbol{\omega}} & \frac{\partial \dot{\mathbf{q}}}{\partial \mathbf{b}} \\ \frac{\partial \dot{\boldsymbol{\omega}}}{\partial \mathbf{q}} & \frac{\partial \dot{\boldsymbol{\omega}}}{\partial \boldsymbol{\omega}} & \frac{\partial \dot{\boldsymbol{\omega}}}{\partial \mathbf{b}} \\ \frac{\partial \dot{\mathbf{b}}}{\partial \mathbf{q}} & \frac{\partial \dot{\mathbf{b}}}{\partial \boldsymbol{\omega}} & \frac{\partial \dot{\mathbf{b}}}{\partial \mathbf{b}} \end{bmatrix} = \begin{bmatrix} \frac{\partial \dot{\mathbf{q}}}{\partial \mathbf{q}} & \frac{\partial \dot{\mathbf{q}}}{\partial \boldsymbol{\omega}} & \mathbf{0}_{4\times3} \\ \mathbf{0}_{3\times4} & \frac{\partial \dot{\boldsymbol{\omega}}}{\partial \boldsymbol{\omega}} & \mathbf{0}_{3\times3} \\ \mathbf{0}_{3\times4} & \mathbf{0}_{3\times3} & \mathbf{0}_{3\times3} \end{bmatrix} \tag{2.45}$$

here,

$$\frac{\partial \dot{\mathbf{q}}}{\partial \mathbf{q}} = \frac{1}{2}\boldsymbol{\Omega}\left(\boldsymbol{\omega}_{meas} - \mathbf{b}\right) - \frac{1}{2}\boldsymbol{\Omega}\left(R_{Local}^{Body}\boldsymbol{\omega}_{EL}^{L}\right) - \frac{1}{2}\boldsymbol{\Omega}\left(\frac{R_{Local}^{Body}}{\partial \mathbf{q}}\boldsymbol{\omega}_{EL}^{L}\right)\mathbf{q}$$

$$\frac{\partial \dot{\mathbf{q}}}{\partial \boldsymbol{\omega}} = \frac{1}{2}\boldsymbol{\Xi}(\mathbf{q})$$

$$\frac{\partial \dot{\boldsymbol{\omega}}}{\partial \boldsymbol{\omega}} = \begin{bmatrix} 0 & -\frac{I_z - I_y}{I_x}\omega_z & -\frac{I_z - I_y}{I_x}\omega_y \\ -\frac{I_x - I_z}{I_y}\omega_z & 0 & -\frac{I_x - I_z}{I_y}\omega_x \\ -\frac{I_y - I_x}{I_z}\omega_y & -\frac{I_y - I_x}{I_z}\omega_x & 0 \end{bmatrix}$$

$$\frac{\partial R_{Local}^{Body}}{\partial q_0} = 2\begin{bmatrix} q_0 & q_3 & -q_2 \\ -q_3 & q_0 & q_1 \\ q_2 & -q_1 & q_0 \end{bmatrix}, \quad \frac{\partial R_{Local}^{Body}}{\partial q_1} = 2\begin{bmatrix} q_1 & q_2 & q_3 \\ q_2 & -q_1 & q_0 \\ q_3 & -q_0 & -q_1 \end{bmatrix}$$

$$\frac{\partial R_{Local}^{Body}}{\partial q_2} = 2\begin{bmatrix} -q_2 & q_1 & -q_0 \\ q_1 & q_2 & q_3 \\ q_0 & q_3 & -q_2 \end{bmatrix}, \quad \frac{\partial R_{Local}^{Body}}{\partial q_3} = 2\begin{bmatrix} -q_3 & q_0 & q_1 \\ -q_0 & -q_3 & q_2 \\ q_1 & q_2 & q_3 \end{bmatrix}$$

Likewise, input matrix G and noise matrix Γ are also linearized in the same way.

$$G = \frac{\partial f}{\partial \mathbf{u}} = \begin{bmatrix} \frac{\partial \dot{\mathbf{q}}}{\partial \mathbf{u}} & \frac{\partial \dot{\boldsymbol{\omega}}}{\partial \mathbf{u}} & \frac{\partial \dot{\mathbf{b}}}{\partial \mathbf{u}} \end{bmatrix}^T \tag{2.46}$$

here,

$$\frac{\partial \dot{\mathbf{q}}}{\partial \mathbf{u}} = \mathbf{0}_{4\times3} \qquad \frac{\partial \dot{\boldsymbol{\omega}}}{\partial \mathbf{u}} = \begin{bmatrix} 0 & \frac{B_x}{I_x} & -\frac{B_y}{I_x} \\ -\frac{B_z}{I_y} & 0 & \frac{B_x}{I_y} \\ \frac{B_y}{I_z} & -\frac{B_x}{I_z} & 0 \end{bmatrix} \qquad \frac{\partial \dot{\mathbf{b}}}{\partial \mathbf{u}} = \mathbf{0}_{3\times3}$$

$$\Gamma = \frac{\partial \mathbf{w}}{\partial \boldsymbol{\eta}} = \begin{bmatrix} \mathbf{0}_{4\times4} & \mathbf{0}_{4\times3} & \mathbf{0}_{4\times3} \\ \mathbf{0}_{3\times4} & I_{3\times3} & \mathbf{0}_{3\times3} \\ \mathbf{0}_{3\times4} & \mathbf{0}_{3\times3} & I_{3\times3} \end{bmatrix} \tag{2.47}$$

By deriving the observation matrix H from the measurement equation, the derivation of extended Kalman filter algorithm ends. The observation matrix can be obtained by partial differentiation for each states.

$$H = \frac{\partial h(\mathbf{x})}{\partial \mathbf{x}} = \begin{bmatrix} \frac{\partial h(\mathbf{x})}{\partial \hat{\mathbf{q}}} & \frac{\partial h(\mathbf{x})}{\partial \hat{\boldsymbol{\omega}}} & \frac{\partial h(\mathbf{x})}{\partial \hat{\mathbf{b}}} \end{bmatrix} \tag{2.48}$$

here,

$$\frac{\partial h(\mathbf{x})}{\partial \mathbf{q}} = \begin{bmatrix} \frac{\partial}{\partial q_0} R_{Local}^{Body} R_{ECI}^{Local} R_{ECEF}^{ECI} R_{NED}^{ECEF} \frac{\mathbf{B}_{IGRF}}{|\mathbf{B}_{IGRF}|} & \cdots & \frac{\partial}{\partial q_3} R_{Local}^{Body} R_{ECI}^{Local} R_{ECEF}^{ECI} R_{NED}^{ECEF} \frac{\mathbf{B}_{IGRF}}{|\mathbf{B}_{IGRF}|} \\ \frac{\partial}{\partial q_0} R_{Local}^{Body} R_{ECI}^{Local} \mathbf{s}_{DE405} & \cdots & \frac{\partial}{\partial q_3} R_{Local}^{Body} R_{ECI}^{Local} \mathbf{s}_{DE405} \\ \mathbf{0} & \cdots & \mathbf{0} \end{bmatrix}$$

$$\frac{\partial h(\mathbf{x})}{\partial \boldsymbol{\omega}} = \begin{bmatrix} \mathbf{0}_{3\times3} \\ \mathbf{0}_{2\times3} \\ \mathbf{I}_{3\times3} \end{bmatrix} \qquad \frac{\partial h(\mathbf{x})}{\partial \mathbf{b}} = \begin{bmatrix} \mathbf{0}_{3\times3} \\ \mathbf{0}_{2\times3} \\ \mathbf{I}_{3\times3} \end{bmatrix}$$

2.7. Attitude Control Algorithm

LQR controller is designed from the estimated attitude information in extended Kalman filter. The states of LQR controller consist of Euler angles and body-fixed angular velocitiy.

$$\mathbf{x}_c = \begin{bmatrix} \phi & p & \theta & \delta q & \psi & r \end{bmatrix}^T, \ \mathbf{u} = \boldsymbol{\mu} = \begin{bmatrix} \mu_x & \mu_y & \mu_z \end{bmatrix}^T \tag{2.49}$$

$\delta q = q + n$, which is designed to a controller for maintaining the mean motion. It means that the cube-satellite maintains the center of the earth.

The system for constructing LQR controller is as follows.

$$\dot{\mathbf{x}}_c = A\mathbf{x}_c + B\mathbf{u} \tag{2.50}$$

here,

$$A=\begin{bmatrix} 0 & 1 & 0 & 0 & n & 0 \\ \frac{3n^2(I_z-I_y)}{I_x} & 0 & 0 & 0 & 0 & \frac{n(I_z-I_y)}{I_x} \\ 0 & 0 & 0 & 1 & 0 & 0 \\ 0 & 0 & \frac{3n^2(I_z-I_y)}{I_y} & 0 & 0 & 0 \\ -n & 0 & 0 & 0 & 0 & 1 \\ 0 & \frac{n(I_y-I_x)}{I_z} & 0 & 0 & 0 & 0 \end{bmatrix}$$

$$B=\begin{bmatrix} 0 & 0 & 0 \\ 0 & \frac{B_z}{I_x} & -\frac{B_y}{I_x} \\ 0 & 0 & 0 \\ -\frac{B_z}{I_y} & 0 & \frac{B_x}{I_y} \\ 0 & 0 & 0 \\ \frac{B_y}{I_z} & -\frac{B_x}{I_z} & 0 \end{bmatrix}$$

Since the input matrix B changes with the geomagnetic field, the control gain is calculated by the following cost functions at each measurement interval. A steady−state is assumed to facilitate implementation convenience.

$$J = \frac{1}{2}\int_0^\infty \mathbf{x}_c(t)^T A\mathbf{x}_c(t) + \mathbf{u}(t)^T B\mathbf{u}(t)dt \tag{2.51}$$

$$K_c(t) = R_c^{-1}B(t)^T P(t),\ \mathbf{u}(t) = -K_c(t)\mathbf{x}_c(t) \tag{2.52}$$

Where P is the solution of the following algebraic Riccati equation.

$$\dot{P}_\infty = 0,\ A^T P + PA - PBR_c^{-1}B^T P + Q_c = 0 \tag{2.53}$$

Chapter 3

A Solution for Magnetic Distortion of Cube-Satellite

SNUGLITE cube-satellite is assembled in compact 2U size with modules such as OBC, EPS, Boom, etc. for mission. It has the advantage of carrying out their mission as an ultra-compact structure, but internal interference between modules due to dense space occurs. A typical problem in SNUGLITE is that the current generated during charging in a solar panel causes a problem. When a cube satellite arrives in the solar period, current flows through the solar panel. The current flowing in a solar panel can flow up to 0.5 amperes per side. Therefore, the current flowing in three-axes panels is more than 1 ampere. This is not a negligible amount of current. This is because the current flowing in the solar panel generates a magnetic field, which is a cause of a serious error in ADCS performance. In addition, magnetic field distortion occurs due to the influence of temperature and metal components of the cube-satellite. These magnetic field distortions can be classified into two types. The first is distortion of the magnetic field measurement, which causes estimation error. The second is magnetic field disturbance, also called residual dipole moment. This causes a control

error. Therefore, this chapter describes how to solve the above-mentioned magnetic field distortion in SNUGLITE cube-satellite. First, temperature, current, and metal compensation are performed to compensate for the magnetic field measurement distortion. In addition, ADCS performance will be verified by modeling the residual dipole moment that induces control error and assigning it to the simulation.

3.1. Magnetometer Calibration for Time-varying Bias

3.1.1. Temperature Calibration

The first consideration is the change in the magnetic field measurements over temperature. In general, MEMS sensor measurements are affected by temperature. Especially, in the space environment, the temperature changes greatly depending on the presence or absence of the sun. In the case of a gyroscope, which is a MEMS sensor mounted on SNUGLITE, the influence of temperature is reflected by estimating bias as a state of EKF. However, magnetometer measurements do not change very much with temperature, such as a gyro. Therefore, the influence of the temperature compensation of the magnetic field sensor is easily distinguished by the temperature scale factor and the bias drift.

At the current temperature (T), the magnetic field measurements for a reference temperature (T_c) can be written as [19]:

$$\begin{aligned} B_{meas}^{T} &= (s_0 + s_1 T) B_{temp}^{T_c} + (b_0 + b_1 T) \\ &= s(T) B_{temp}^{T_c} + b(T) \end{aligned} \tag{3.1}$$

$$T = T_c + \Delta T \tag{3.2}$$

Therefore, if the magnetic field measurements are compensated based on a reference temperature (T_c), the following Equation 3.3 is obtained.

$$\begin{aligned} B_{temp}^{T_c} &= \frac{B_{meas}^{T} - b(T)}{s(T)} \\ &= \frac{B_{meas}^{T} - (b_0 + b_1 T)}{s_0 + s_1 T} \end{aligned} \tag{3.3}$$

However, the bias term is neglected because the effect on bias due to temperature is negligible. And Equation 3.3 is simplified as follows.

$$\begin{aligned} B_{temp}^{T_c} &\approx \frac{B_{meas}^{T}}{s(T)} \\ &\approx \frac{B_{meas}^{T}}{s_0 + s_1 T} \end{aligned} \tag{3.4}$$

The temperature compensation equation for the 3-axis magnetic field measurement is Equation 3.5.

$$\mathbf{B}_{temp}^{T_c} = \begin{bmatrix} B_{temp,x}^{T_c} \\ B_{temp,y}^{T_c} \\ B_{temp,z}^{T_c} \end{bmatrix} = \begin{bmatrix} \dfrac{B_{meas,x}^{T}}{s_x(T)} \\ \dfrac{B_{meas,y}^{T}}{s_y(T)} \\ \dfrac{B_{meas,z}^{T}}{s_z(T)} \end{bmatrix} \tag{3.5}$$

The temperature change on the orbit is from −20 to 50 degrees, and the reference temperature (T_c) is set to 25 degrees. The solar period is 64% (about 1 hour) and the solar eclipse period is 36% (about 35 minutes).

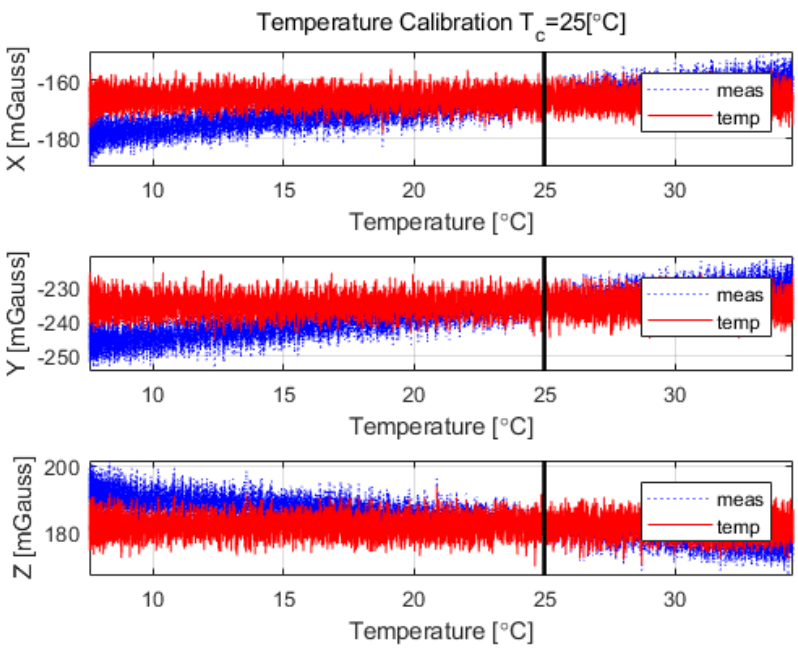

Figure 3.1: Results of Temperature Compensation

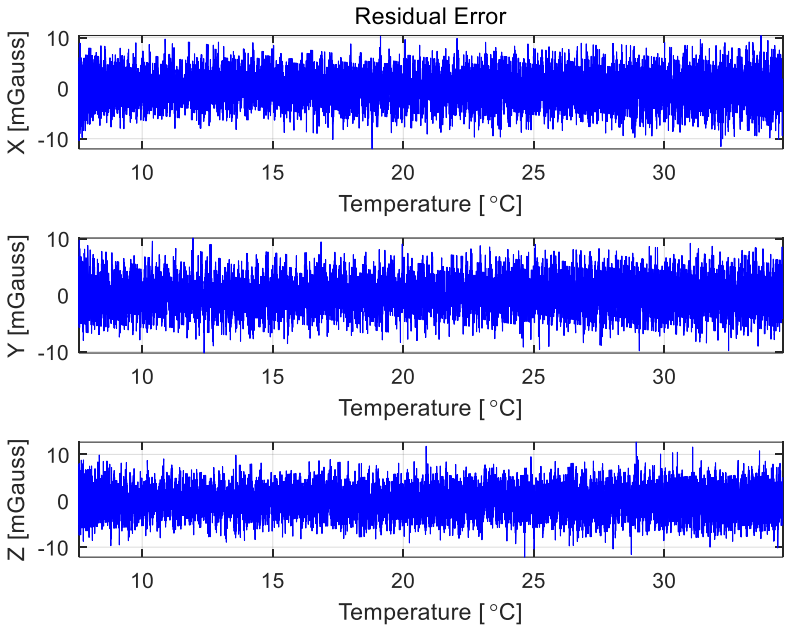

Figure 3.2: Temperature Compensation Residual Error

Table 3.1: Temperature Scale Factor Components

Scale Factor	x−axis	y−axis	z−axis
$s_0[*]$	1.11	1.07	1.08
$s_1[*]/[^\circ C]$	-4.33×10^{-3}	-2.73×10^{-3}	-3.03×10^{-3}

Table 3.2: Residual Error After Temperature Compensation

Residual	x−axis	y−axis	z−axis
RMS [*mGauss*]	2.91	2.67	2.81

From the results in Table 3.2, it can be seen that the RMS of residual error after temperature compensation is about 3 milli-gauss. Considering that the standard deviation of the magnetic field sensor is 3 milli-gauss, the temperature compensation is deemed appropriate.

3.1.2. Current Compensation

One of the differences between the EM and FM used in the SNUGLITE ADCS study is the presence or absence of solar panels.

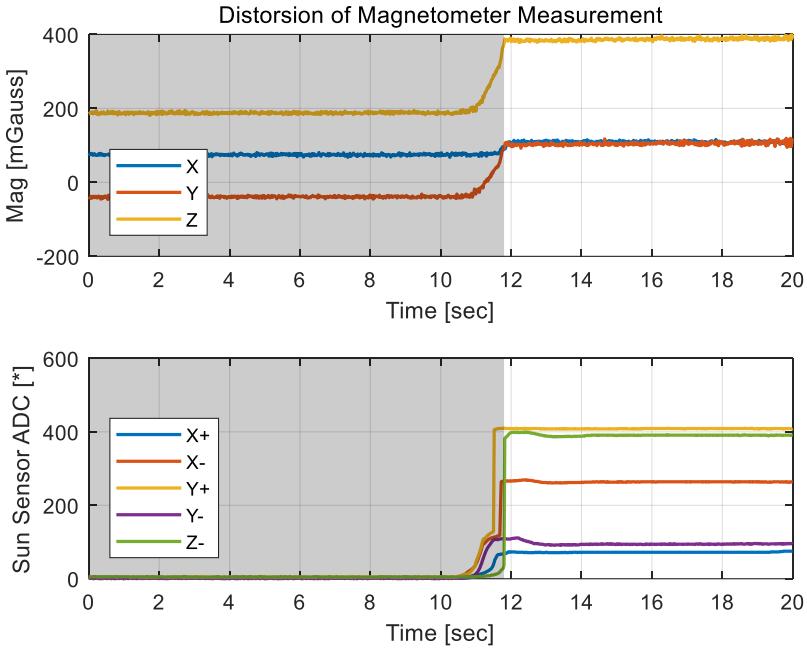

Figure 3.3: Distortion of Magnetic field Measurements by Solar Panels (Black: Eclipse)

As a result, the measured value of the magnetic field sensor is distorted by the solar panel in FM. As shown in Figure 3.3, it can be seen that the magnetic field measurements are changing when the sun rises. It is interpreted that when the current flows through the solar panel by the sunlight, the distortion of magnetic field measurement is caused.

$$B = \frac{\mu_0 i}{4\pi} \int \frac{d\ell \times \hat{r}}{r^2} \tag{3.6}$$

$d\ell$: vector line element of current direction
r : distance from $d\ell$
$\hat{r}$: unit vector in direction of r
i : current

If the wire that generates the magnetic field is fixed, the magnetic field can be simply summarized as [18], [19]:

$$B = K_s \cdot i \tag{3.7}$$

Therefore, the magnetic field distortion can be compensated from the relationship between the current and the magnetic field. However, SNUGLITE cube-satellite EPS module provides current measurements for each axis. Also, from Figure 3.4, the number of panels differs for the Y+ panel and the Z-panel due to the attachment of the GPS receiver.

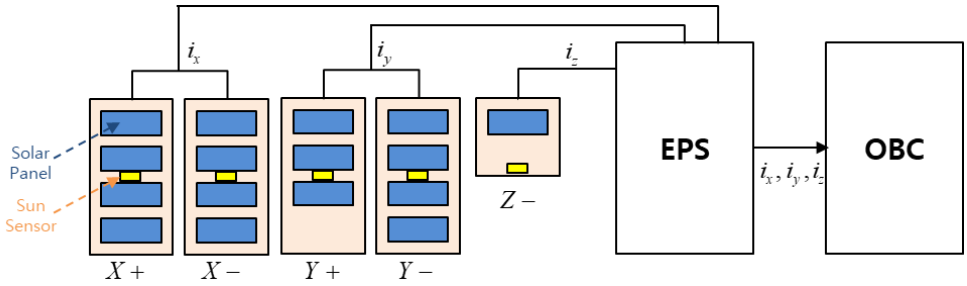

Figure 3.4: Configuration Diagram of Current Measurement

Here, the current measurement of each axis can be written as follows.

$$\mathbf{i} = \begin{bmatrix} i_x \\ i_y \\ i_z \end{bmatrix} = \begin{bmatrix} i_x^+ + i_x^- \\ i_y^+ + i_y^- \\ i_z^- \end{bmatrix} \tag{3.8}$$

To solve this problem, current measurements measured on each panels are distributed using sun sensor measurements. The idea is very simple. First, from the ratio of the sun measurements to the five planes, the currents flowing on each plane are distributed to calculate current measurements for the five planes $\mathbf{i}_5$.

$$\mathbf{s}_{body} = \begin{bmatrix} s_x^+ & s_x^- & s_y^+ & s_y^- & s_z^- \end{bmatrix}^T \tag{3.9}$$

$$i_x^+ = \frac{s_x^+}{s_x^+ + s_x^-} i_x,\ i_x^- = \frac{s_x^-}{s_x^+ + s_x^-} i_x,\ i_y^+ = \frac{s_y^+}{s_y^+ + s_y^-} i_y,\ i_y^- = \frac{s_y^-}{s_y^+ + s_y^-} i_y,\ i_z^- = i_z \tag{3.10}$$

$$\mathbf{i}_5 = \begin{bmatrix} i_x^+ & i_x^- & i_y^+ & i_y^- & i_z^- \end{bmatrix}^T \tag{3.11}$$

The magnetic field measurements for the 5−sided currents are defined as follows:

$$\begin{aligned} \mathbf{B}_{sun}(\mathbf{i}_5) &= \mathbf{B}_{temp}(\mathbf{0}) + \delta\mathbf{B}(\mathbf{i}_5) + \varepsilon \\ &\cong \mathbf{B}_{temp}(\mathbf{0}) + \delta\mathbf{B}(\mathbf{i}_5) \end{aligned} \tag{3.12}$$

A temperature compensated magnetic field measurement $(\mathbf{B}_{temp})$ is a measure of when no current is flowing. That is, it is a measurement that is not distorted by the current. The magnetic field measurements distorted by the current in the solar panel $\delta\mathbf{B}(\mathbf{i}_5)$ are added by the superposition principle. From Equation 3.7, the magnetic field distortion is proportional to the current, so it can be written as the product of the current and the distortion constant.

$$\begin{aligned} \delta\mathbf{B}(\mathbf{i}_5) &= \delta B_x^+(i_x^+) + \delta B_x^-(i_x^-) + \delta B_y^+(i_y^+) + \delta B_y^-(i_y^-) + \delta B_z^-(i_z^-) \\ &= \begin{bmatrix} K_x^{x+} & K_x^{x-} & K_x^{y+} & K_x^{y-} & K_x^{z-} \\ K_y^{x+} & K_y^{x-} & K_y^{y+} & K_y^{y-} & K_y^{z-} \\ K_z^{x+} & K_z^{x-} & K_z^{y+} & K_z^{y-} & K_z^{z-} \end{bmatrix} \begin{bmatrix} i_x^+ \\ i_x^- \\ i_y^+ \\ i_y^- \\ i_z^- \end{bmatrix} \\ &= K_s \cdot \mathbf{i}_5 \end{aligned} \tag{3.13}$$

Unfortunately, when the battery is fully charged, it consumes current in the EPS to avoid charging battery. Then, the battery charging mode is divided into two types: normal and full mode. Depending on the mode, the degree of magnetic field distortion varies. In the case of full mode, the standard deviation of the measured value becomes larger than the normal period, and the magnetic field distortion constant is also different. Therefore, the magnetic field distortion constants for normal and full modes are respectively calculated. To do this, a device is constructed to get the magnetic field distortion constant for each plane as shown in the following figure.

Figure 3.5: Configuration of Magnetic Field Distortion Modeling Device for Current

By using the least squares method, the magnetic field distortion constant according to each mode can be obtained.

$$K_{norm} = \begin{bmatrix} 0.0437 & 0.0508 & 0.0650 & 0.0463 & -0.0171 \\ 0.0350 & 0.0237 & -0.0670 & -0.1618 & 0.5114 \\ 0.0836 & 0.0538 & -0.0195 & -0.0270 & 0.7147 \end{bmatrix} \tag{3.14}$$

$$K_{full} = \begin{bmatrix} 0.0562 & 0.0579 & 0.1049 & 0.1647 & -0.0302 \\ -0.0007 & -0.0207 & 0.0335 & 0.0147 & 0.6558 \\ 0.0627 & 0.0523 & 0.0095 & -0.0333 & 0.8921 \end{bmatrix} \tag{3.15}$$

Therefore, the magnetic field due to the current distortion can be compensated as follows.

$$\mathbf{B}_{curr} = \mathbf{B}_{meas}(\mathbf{i}_5) - \delta\mathbf{B}(\mathbf{i}_5) \tag{3.16}$$

Using Equation 3.16, the results of current compensation according to each mode are shown in Figures 3.6 to 3.7. The references in the figures are the average of the magnetic field measurements when no current flows. It seems appropriate that the distortion due to the current is well compensated by the reference. The results for current compensation are shown in Tables 3.3 and 3.4. Both normal and full modes have less distortion on the x−axis and are dominant on the y− and z−axis. Especially, in full mode, RMS and STD of distortion are found to be similar values because noise is generated which does not follow normal distribution. It is reflected in the measurement noise of EKF with reference to the noise characteristics analyzed in Tables 3.3 and 3.4.

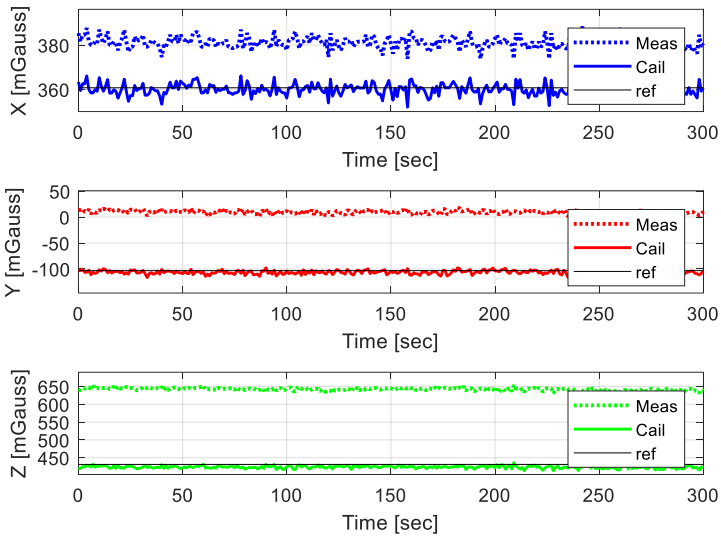

Figure 3.6: Current Compensation Result (Normal Mode)

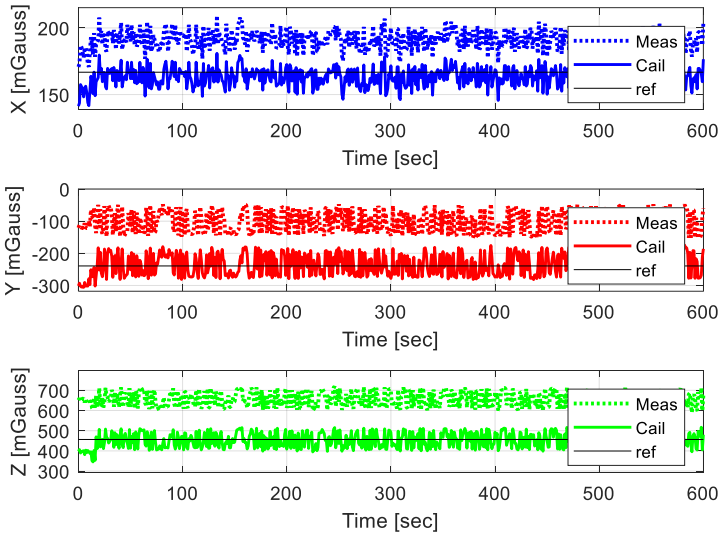

Figure 3.7: Current Compensation Result (Full Mode)

Table 3.3: Residual Error of Current Compensation (Normal Mode)

Residual Error	x-axis [*mGauss*]	y-axis [*mGauss*]	z-axis [*mGauss*]
Bias Mean	4.19	9.59	9.39
Bias RMS	5.63	10.96	11.00
STD	3.76	5.32	5.75

Table 3.4: Residual Error of Current Compensation (Full Mode)

Residual Error	x-axis [*mGauss*]	y-axis [*mGauss*]	z-axis [*mGauss*]
Bias Mean	2.90	3.35	2.07
Bias RMS	6.79	27.29	29.74
STD	6.61	27.29	29.73

3.1.3. Hard-Iron and Soft-Iron Compensation

Distortion of the magnetic field occurs from the metallic material of the cube-satellite. The effect of metal is divided into two kinds. The first is the hard-iron effect, which causes the offset error of the magnetic field measurements by the metal. The second is the distortion of the uniformity of the geomagnetic field in all directions

due to the soft iron effect, which is the ellipsoid error. The ellipsoidal compensation method is used to eliminate these error factors [16], [19]. The magnetic field measurements used for ellipsoid compensation use temperature and current compensated measurements.

Hard-iron compensation is simply a compensation for the offset error and can be written as:

$$\mathbf{B}_{ellip}^{hard} = \mathbf{B}_{curr} - \mathbf{r}_{ellip} \tag{3.17}$$

In the case of soft-iron compensation, the distorted ellipsoid is compensated with a sphere. After hard-iron compensation, the rotation transformation matrix is calculated from the magnetic field measurements, and the scale is unified based on the z-axis measurements. Then, the ellipsoid compensated magnetic field measurements are calculated by multiplying the scale factor errors (sf_{IGRF}) obtained from the IGRF-12 model. Here, the measurements for the actual ellipsoid compensation are obtained outdoors, which can yield a true value from the IGRF-12 model.

$$\mathbf{B}_{ellip}^{phase} = R_{eig}\mathbf{B}_{ellip}^{hard} \tag{3.18}$$

$$\mathbf{B}_{ellip}^{soft} = R_{eig}^{T}\mathbf{B}_{scale} \tag{3.19}$$

where,

$$\mathbf{B}_{scale} = \begin{bmatrix} B_{scale}^{x} \\ B_{scale}^{y} \\ B_{scale}^{z} \end{bmatrix} = \begin{bmatrix} \dfrac{r_{ellip}^{z}}{r_{ellip}^{x}} B_{ellip}^{phase,x} \\ \dfrac{r_{ellip}^{z}}{r_{ellip}^{y}} B_{ellip}^{phase,y} \\ B_{ellip}^{phase,z} \end{bmatrix}$$

$$\mathbf{B}_{iron} = sf_{IGRF} \mathbf{B}_{ellip}^{soft} \tag{3.20}$$

The comparison between before and after application of ellipsoid compensation shows that the effects of hard iron and soft iron are removed as shown in the following figure.

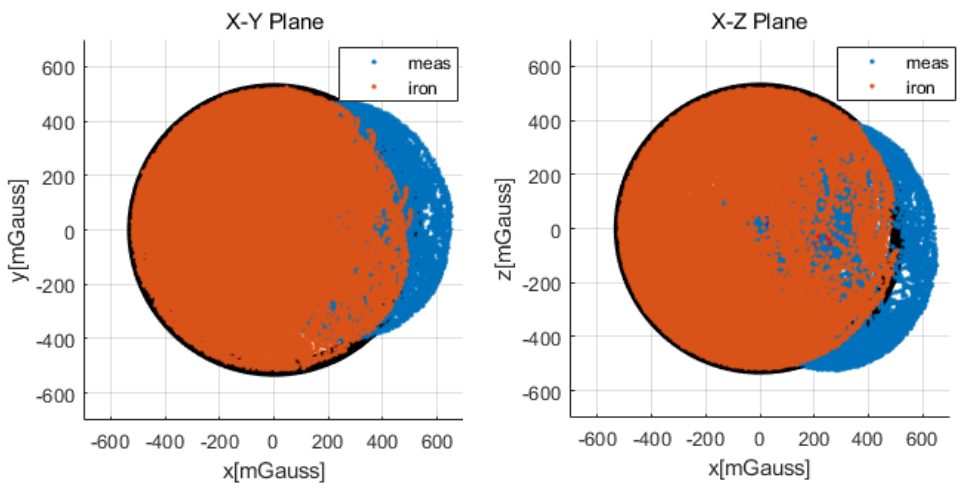

(a) XY Plane (b) XZ Plane

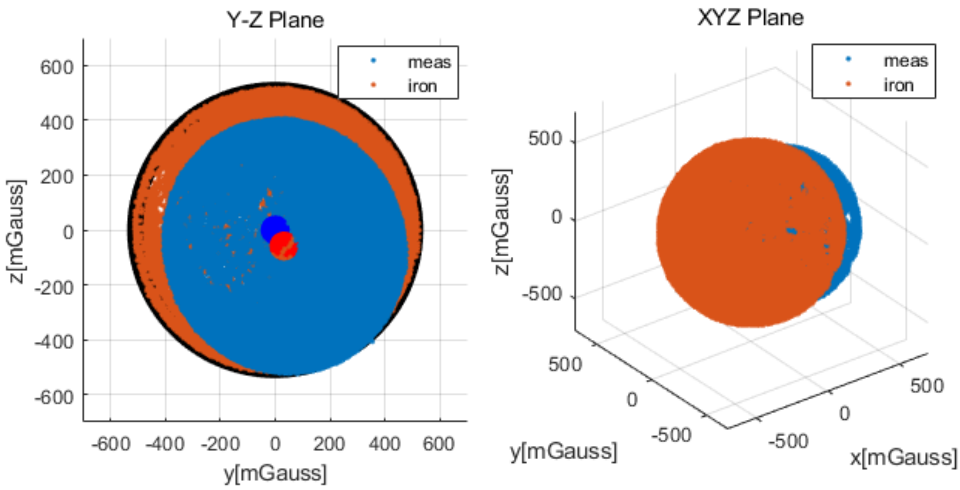

(c) YZ Plane (d) XYZ Plane

Figure 3.8: Results of Ellipsoid Compensation

3.2. Residual Magnetic Dipole Moment

As a second problem of magnetic field distortion, control errors are caused. This is also called residual dipole moment. Low-Earth orbit satellites are in the influence of the geomagnetic field, and currents flowing in the satellites can cause residual dipole moment due to interference with the geomagnetic field. SNUGLITE Cube-satellite modules that consume a lot of current are solar panels and EPS. Therefore, for these two modules, the residual dipole moment must be measured to predict the control performance in space. However, it is difficult to know how the closed loop of the current for the two modules is constructed. For this reason, in this thesis, assuming that

the closed loop of each module is a square wire, the dipole moment is predicted. Since the dipole moment generates a magnetic field, the dipole moment can be predicted by measuring the magnetic field for the current. The relationship between the dipole moment and the magnetic field can be written as [20]:

$$B(\vec{\mu},\vec{r}) = 3\frac{\hat{r}}{r^3}\left(\vec{\mu}\cdot\hat{r}\right) - \frac{\vec{\mu}}{r^3}[mGauss] \tag{3.21}$$

However, in order to use Eq. 3.21, it is necessary to know the closed loop through which the current flows. In this paper, we cannot exactly know the closed loop through which current flows. To solve this problem, numerical analysis is carried out through a magnetic field generated in a closed loop assuming a rectangular, and a residual dipole moment is calculated.

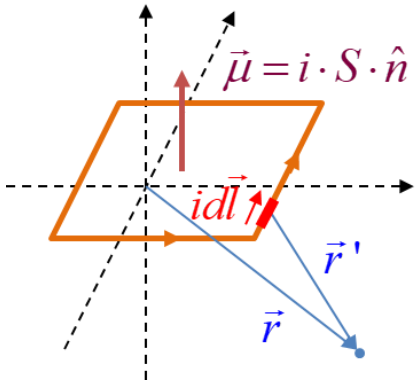

Figure 3.9: Magnetic field measurement for dipole moment modeling

Since the magnetic field generated by the current is indecipherable, a precise magnetic field sensor is needed to measure it. In this paper, a magnetic field sensor of 0.067 milli-gauss resolution is used. As a result, assuming that the closed loop of the solar panel and EPS module is a square wire, the dipole moment is calculated by numerical analysis as shown in the following table. Here, the current through the solar panel is up to 0.5 amperes, when the sun is vertical on one side.

Table 3.5: Maximum Residual Dipole Moment of Modules

Module	Maximum Dipole Moment
Solar Panel	$1.31\times10^{-3}\ [A\cdot m^2]$
EPS	$2.10\times10^{-3}\ [A\cdot m^2]$

Solar Panel and EPS are assembled vertically. Therefore, the maximum residual dipole moment of SNUGLITE is calculated by the following Eq. 3.22 based on the geometric relationship in the Figure 3.10.

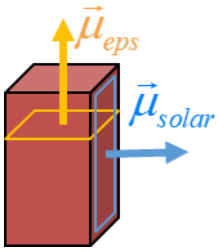

Figure 3.10: Geometric Relationship of the Residual Dipole Moment

$$\begin{aligned}\mu_{resid}^{\max} &= \sqrt{\mu_{solar}^2 + \mu_{eps}^2} \\ &= 2.48\times10^{-3}\ [A\cdot m^2]\end{aligned} \tag{3.22}$$

The calculated maximum residual dipole moment is about 6% of the maximum dipole moment of magnetorquer, which is an insufficient force. Also, the current of the solar panel changes according to the attitude of the cube-satellite and the value of the residual dipole moment changes. For this reason, it is not easy to calculate the control input compensated for this. Therefore, the maximum residual dipole moment is reflected as process noise of EKF, and it is considered as disturbance for dynamics.

3.3. Simulation

3.3.1. Simulation Envirionment

Space environment simulations are essential to verify ADCS of the cube-satellite. Especially, since the space environment is difficult to simulate equally on the ground, a sophisticated space environment should be modeled and simulated. In addition, the implemented algorithm of the OBC should be verified. To do this, Software-In-the-Loop Simulation and Processor-In-the-Loop Simulation (PILS) must be performed through separation of space environment and

ADCS algorithm. SILS and PILS have been performed in previous studies [15], [32]. This chapter is an extension of previous researches, and simulation considering magnetic field distortion is considered.

SILS and PILS are configured to receive measurements from the same space environment as shown in the following Figure 3.11.

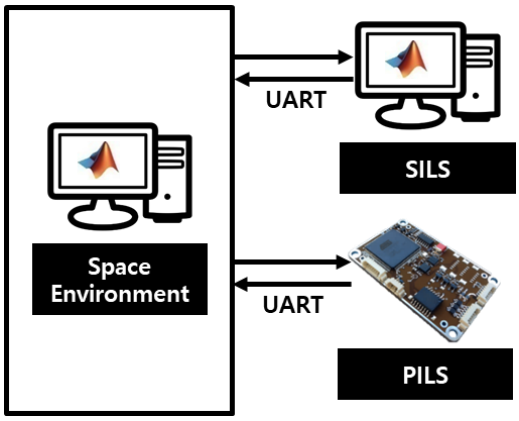

Figure 3.11: Configuration of SILS and PILS

As shown in the figure, UART communication is used to exchange data between the separated space environment and ADCS algorithm of the cube-satellite. In the case of ADCS, the design model is used by approximation and linearization. In order to apply it to the space environment, the elaborate model is simulated considering the actual disturbance factors. The models used for space environment and ADCS are shown in the following table [14].

Table 3.6: Models Used in Space Environment and ADCS

–	Space	ADCS
Moment of Inertia	$I_{xy}, I_{yz}, I_{zx} \neq 0$	$I_{xy} = I_{yz} = I_{zx} = 0$
Gravity Model	Two Body Equation, J2 Effect	Two Body Equation
Air Drag Density	Harris−Priester Model	EKF Noise Process Noise
Solar Radiation Pressure Model	Spherical Shedow Model	
Magnetic Field	IGRF−12 (Full order)	IGRF−12 (Reduced 11th order)
Solar System Model	JPL−DE405 Model	Simplified Polynomial Model
Residual Dipole Moment	1st−order Gauss Markov Process	EKF Process Noise

The process noise of EKF in Eq. 2.40 assumed in the table is set as follows.

$$\sigma_{gg} = \frac{3\mu_e}{2r^3}\sin(2\theta) \times \frac{I_x - I_z}{I_y} = 1.1459 \times 10^{-6}\,[rad/s^2]$$

$$\sigma_{sr} = \frac{F_s}{c} A(1+q)\frac{x}{I_y} = 0$$

$$\sigma_{ad} = \frac{\rho}{2} v_{rel}^2 C_d \frac{A}{I_y} x = 0$$

$$\sigma_{mdt} = \frac{\left|\mu_{resid}^{\max}\right|\left|B\right|}{I_z} = 3.78 \times 10^{-5}\ [rad/s^2]$$

$$\sigma_{rrw} = 6.9813 \times 10^{-5}\,[rad/s^2]$$

here, the process noise for the solar radiation pressure (σ_{sr}) and air drag changes (σ_{ad}) when the boom is deployed, where $x = 0.03\,[m]$.

All measurements generated in the space are passed to the ADCS, which adds noise to each sensor specification. Orbital information and initial conditions on the cube-satellite are as follows.

Table 3.7: Keplerian Orbit Elements

Parameters	Values
Semi-major Axis (a)	6978 $[km]$
Eccentricity (e)	0.01
Right Ascension (Ω)	18 [deg]
Inclination Angle (i)	98 [deg]
Argument of Perigee (ω)	0 [deg]
True Anomaly (ν)	0 [deg]

Table 3.8: Initial Condition of Simulation

ϕ	θ	ψ	p	q	r
0 [deg]	0 [deg]	0 [deg]	10 [deg/ s]	10 [deg/ s]	10 [deg/ s]

In the case of the initial condition, it is set based on when the cube-satellite is ejected from the p-pod. Since the magnitude of the maximum angular velocity at the time of ejection is 15 degrees per seconds, the angular velocity is set to 10 degrees per seconds on each axis. The attitude is an arbitrary, all are set to zero.

To reflect the magnetic field distortion in the simulation, noise and residual bias calculated in Chap 3.1 were added to the magnetic field measurement as follows. Here, it is assumed that magnetic field distortion does not occur during the eclipse period.

Table 3.9: Distortion of Magnetic Measurement in Simulation

Mode	Standard Deviation [*mGauss*]			Residual Bias [*mGauss*]		
	x-axis	y-axis	z-axis	x-axis	y-axis	z-axis
Solar (Normal)	4	5	6	4	10	10
Solar (Full)	7	27	30	3	3	2
Eclipse	4	4	4	0	0	0

The measured values of EKF considering the magnetic field distortion vary depending on each mode. It is divided into the solar and eclipse periods, estimation only, estimation and control mode, battery charging, and passing through polar regions where the magnetic field changes abruptly. Depending on the mode, the number of available measurements varies. Accordingly, EKF estimates the attitude of the cube-satellite. The measurement noise setting for each mode is shown in the following table.

Table 3.10: Extended Kalman Filter Measurement Noise

Mode		Solar Period		Eclipse
		3−Axis Sun Vector	2−Axis Sun Vector	
Estimation Only	Normal	$R_{est}^{norm3} = \begin{bmatrix} \frac{\sigma_{mag,normal}^2}{\lvert \mathbf{B}_{IGRF} \rvert^2} I_{3\times3} & \mathbf{0} & \mathbf{0} \\ \mathbf{0} & \sigma_{sun}^2 I_{3\times3} & \mathbf{0} \\ \mathbf{0} & \mathbf{0} & \sigma_{arw}^2 I_{3\times3} \end{bmatrix}$	$R_{est}^{norm2} = \begin{bmatrix} \frac{\sigma_{mag,normal}^2}{\lvert \mathbf{B}_{IGRF} \rvert^2} I_{3\times3} & \mathbf{0} & \mathbf{0} \\ \mathbf{0} & \sigma_{sun}^2 I_{2\times2} & \mathbf{0} \\ \mathbf{0} & \mathbf{0} & \sigma_{arw}^2 I_{3\times3} \end{bmatrix}$	$R_{est}^{ecl} = \begin{bmatrix} \frac{\sigma_{mag,eclipse}^2}{\lvert \mathbf{B}_{IGRF} \rvert^2} I_{3\times3} & \mathbf{0} \\ \mathbf{0} & \sigma_{arw}^2 I_{3\times3} \end{bmatrix}$
	Full	$R_{est}^{full3} = \begin{bmatrix} \frac{\sigma_{mag,full}^2}{\lvert \mathbf{B}_{IGRF} \rvert^2} I_{3\times3} & \mathbf{0} & \mathbf{0} \\ \mathbf{0} & \sigma_{sun}^2 I_{3\times3} & \mathbf{0} \\ \mathbf{0} & \mathbf{0} & \sigma_{arw}^2 I_{3\times3} \end{bmatrix}$	$R_{est}^{full2} = \begin{bmatrix} \frac{\sigma_{mag,full}^2}{\lvert \mathbf{B}_{IGRF} \rvert^2} I_{3\times3} & \mathbf{0} & \mathbf{0} \\ \mathbf{0} & \sigma_{sun}^2 I_{2\times2} & \mathbf{0} \\ \mathbf{0} & \mathbf{0} & \sigma_{arw}^2 I_{3\times3} \end{bmatrix}$	
	Pole	$R_{est}^{pole3} = \begin{bmatrix} \frac{\sigma_{mag,pole}^2}{\lvert \mathbf{B}_{IGRF} \rvert^2} I_{3\times3} & \mathbf{0} & \mathbf{0} \\ \mathbf{0} & \sigma_{sun}^2 I_{3\times3} & \mathbf{0} \\ \mathbf{0} & \mathbf{0} & \sigma_{arw}^2 I_{3\times3} \end{bmatrix}$	$R_{est}^{pole2} = \begin{bmatrix} \frac{\sigma_{mag,pole}^2}{\lvert \mathbf{B}_{IGRF} \rvert^2} I_{3\times3} & \mathbf{0} & \mathbf{0} \\ \mathbf{0} & \sigma_{sun}^2 I_{2\times2} & \mathbf{0} \\ \mathbf{0} & \mathbf{0} & \sigma_{arw}^2 I_{3\times3} \end{bmatrix}$	$R_{est}^{pole,e} = \begin{bmatrix} \frac{\sigma_{mag,pole}^2}{\lvert \mathbf{B}_{IGRF} \rvert^2} I_{3\times3} & \mathbf{0} \\ \mathbf{0} & \sigma_{arw}^2 I_{3\times3} \end{bmatrix}$
Estimation and Control		$R_{ctl}^{sun} = \begin{bmatrix} \sigma_{sun}^2 I_{3\times3} & \mathbf{0} \\ \mathbf{0} & \sigma_{arw}^2 I_{3\times3} \end{bmatrix}$		$R_{ctl}^{ecl} = \sigma_{arw}^2 I_{3\times3}$

here,

$$\sigma_{sun} = diag\begin{bmatrix}3 & 3 & 3\end{bmatrix}[\text{deg}] \qquad \sigma_{mag,normal} = diag\begin{bmatrix}6 & 11 & 11\end{bmatrix}\times10^{-7}\,[T]$$

$$\sigma_{arw} = diag\begin{bmatrix}0.02 & 0.02 & 0.02\end{bmatrix}[\text{deg}/s] \qquad \sigma_{mag,full} = diag\begin{bmatrix}7 & 27 & 30\end{bmatrix}\times10^{-7}\,[T]$$

$$\sigma_{mag,eclipse} = diag\begin{bmatrix}4 & 4 & 4\end{bmatrix}\times10^{-7}\,[T] \qquad \sigma_{mag,pole} = 1000\times\sigma_{mag,eclipse}$$

3.3.2. Results

The simulation was performed according to the following operational scenarios.

1) The total simulation time is 48 hours.
2) The boom is deployed after 24 hours, and the moment of inertia of the cube satellite changes.
3) The residual dipole moment is applied in the worst case to predict the worst performance of the ADCS.
4) In the battery scenario, 20% of the solar period is set as the charging period, and the buffer period in which the magnetic field distortion is large is set long.

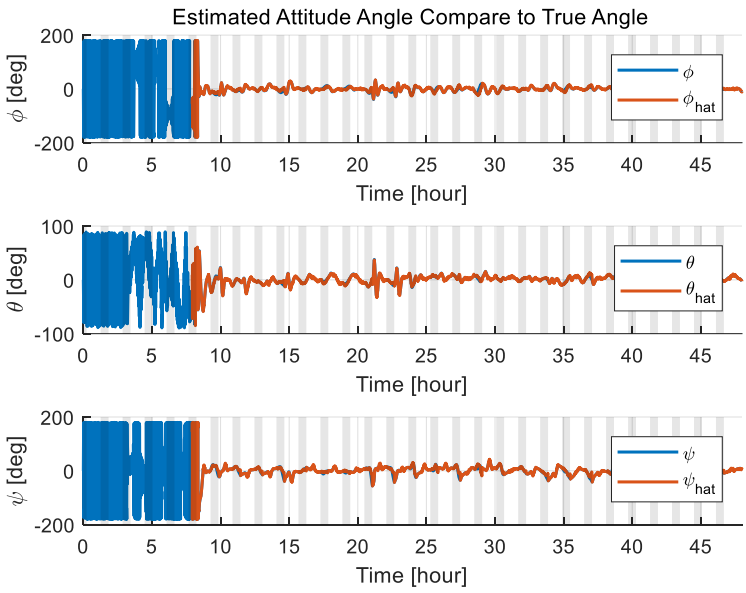

Figure 3.12: Worst Case SILS Results

Euler Angles for the Entire Operation Scenario

In Figure 3.12, the angular velocity attenuation mode proceeds until the initial 8 hours. In this case, estimation of the attitude angle is not performed. When the angular velocity attenuation is completed, the mission mode is immediately executed and the boom develops after about 24 hours. The black box in the figures indicates the eclipse.

First, the performance of the angular velocity attenuation mode is shown in Figure 3.13. The angular velocity shown in the figure is a true value. Since the magnetic field change rate is calculated in the angular velocity attenuation mode, the true values of the angular velocity cannot be calculated.

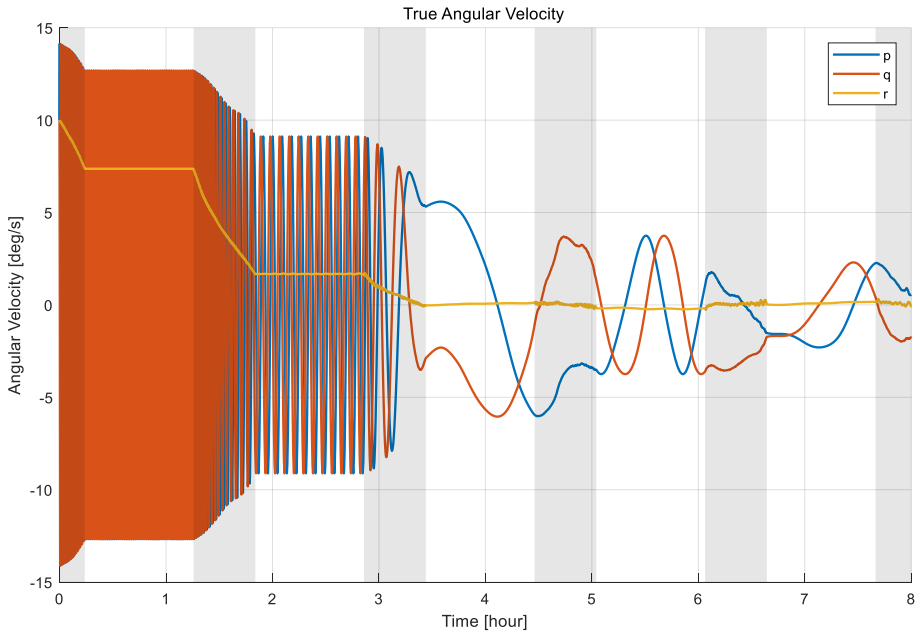

Figure 3.13: Angular Velocity of
the Angular Velocity Attenuation Mode (B-dot Control)

In the case of angular velocity attenuation mode, magnetic field measurement is used, which is fatal to magnetic field distortion. Therefore, for stability of angular velocity attenuation, it is designed to be performed only in case of eclipse. Figure 3.13 shows that angular velocity is not changed during the solar period. Here, the angular velocity for roll and pitch is sinusoidal due to gravity gradient torque. The angular velocity attenuation mode is converted to mission mode when the angular velocity reaches 0.3 degree per seconds.

Next, the mission mode and the boom deployment mode are shown by Euler angle, angular velocity, and gyro bias, respectively. In case of quaternion, which is a state of EKF, it is difficult to interpret, so it is converted into Euler angles and its performance is verified. The simulation performance of ADCS is appended to the worst case magnetic field distortion, so it can be predicted that it is the worst performance in the earth oriented attitude. When there is a magnetic field distortion, the nadir-pointing attitude requirement performance is set as follows.

1) Control Performances:

   RMS of $\phi, \theta < 10\ [\mathrm{deg}]$, RMS of $\psi < 15\ [\mathrm{deg}]$

2) Estimation Performances:

   According to the stochastic definition of EKF, it should be included in the 3-sigma bounding of standard deviation.

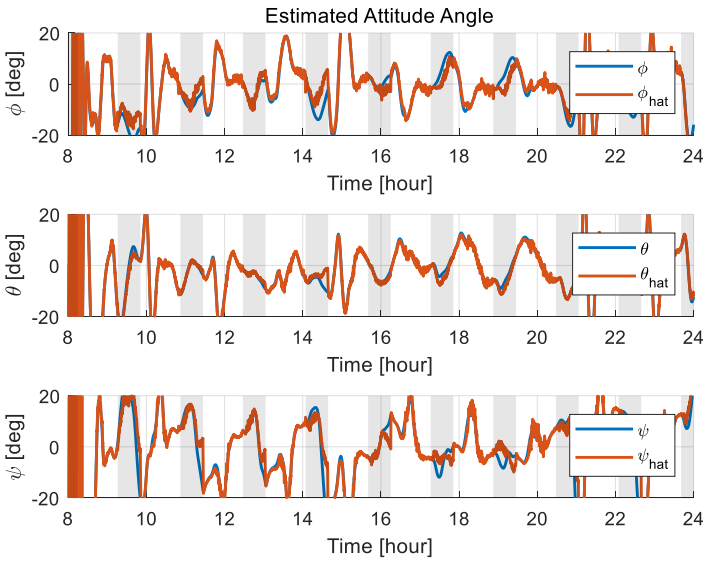

Figure 3.14: Worst Case Simulation Results

– Euler Angle (Mission Mode)

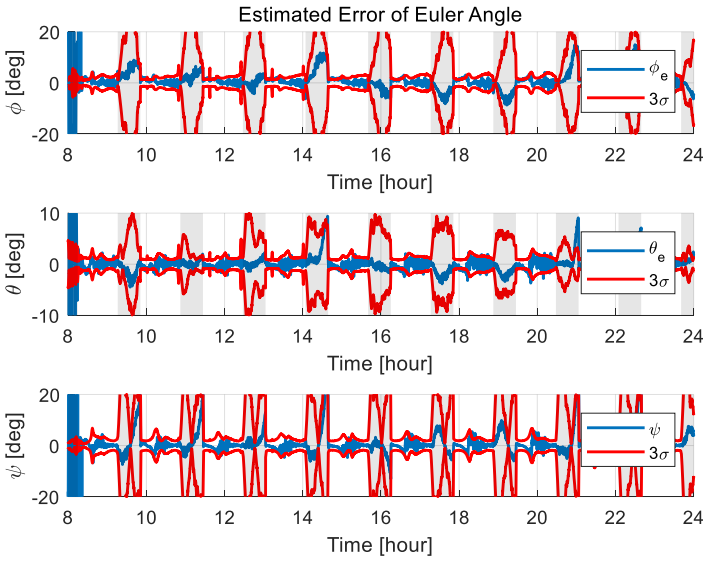

Figure 3.15: Estimation Error

– Euler Angle (Mission Mode)

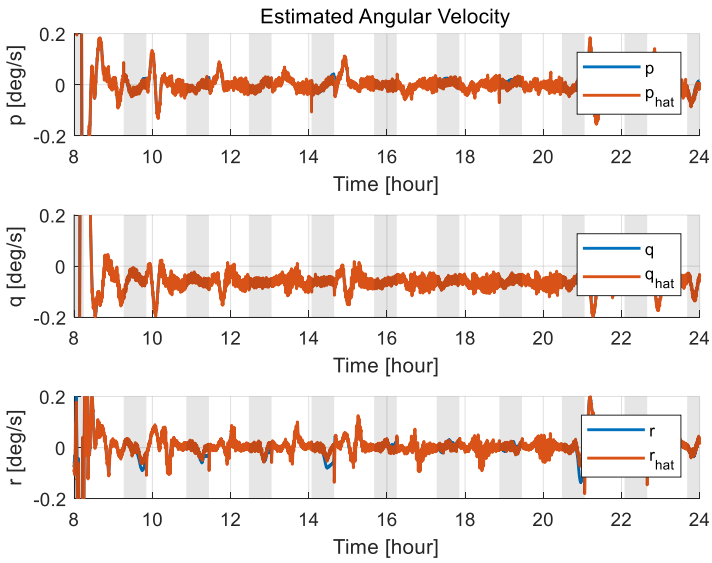

Figure 3.16: Worst Case Simulation Results

– Angular Velocity (Mission Mode)

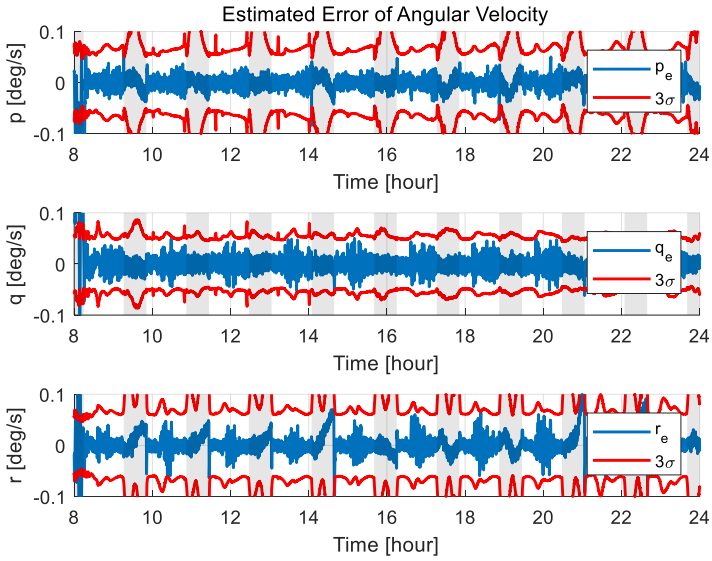

Figure 3.17: Estimation Error

– Angular Velocity (Mission Mode)

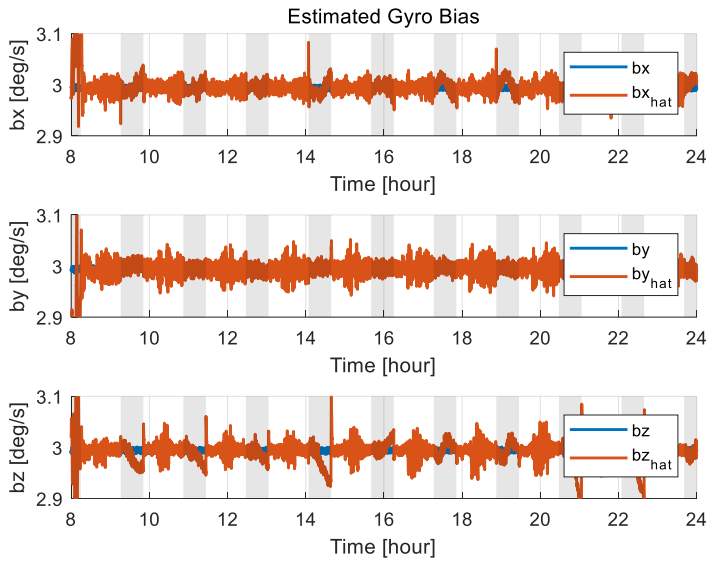

Figure 3.18: Worst Case Simulation Results

– Gyro Bias (Mission Mode)

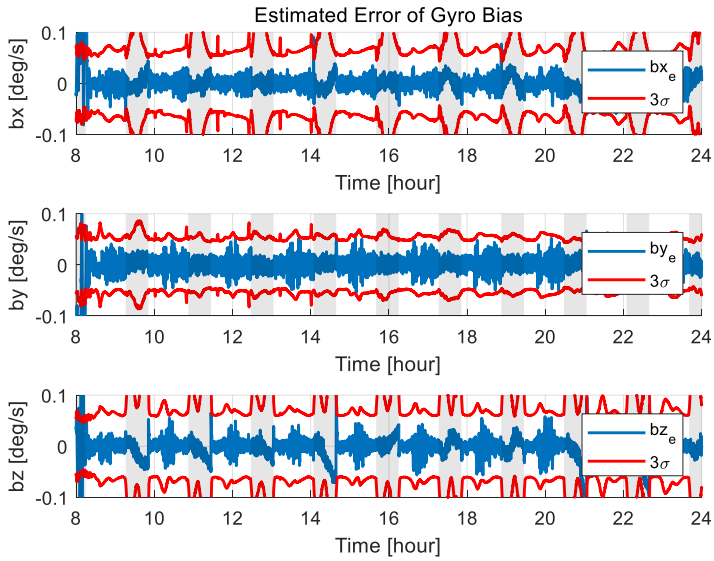

Figure 3.19: Estimation Error

– Gyro Bias (Mission Mode)

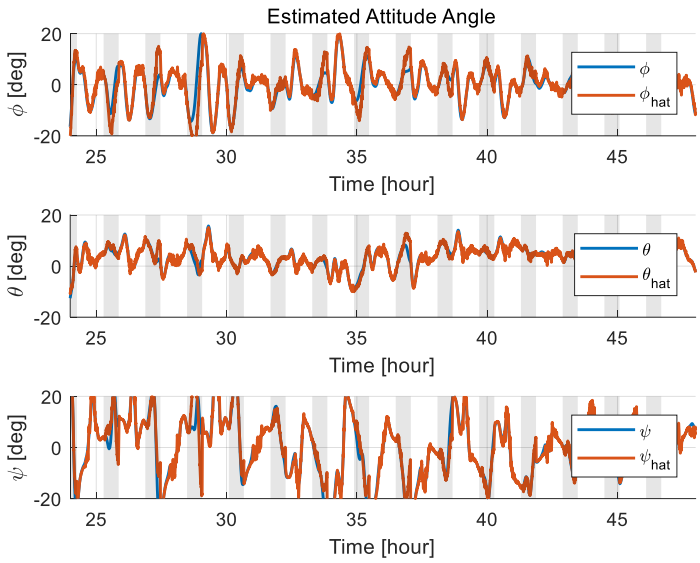

Figure 3.20: Worst Case Simulation Results

– Euler Angle (Boom Deployed)

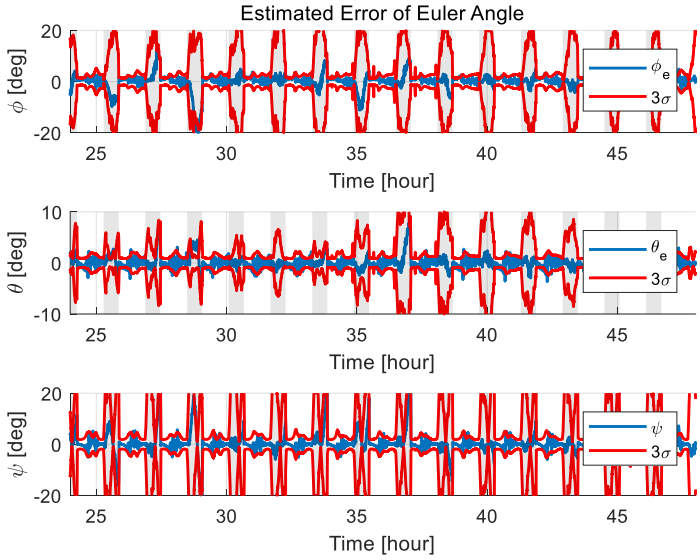

Figure 3.21: Estimation Error

– Euler Angle (Boom Deployed)

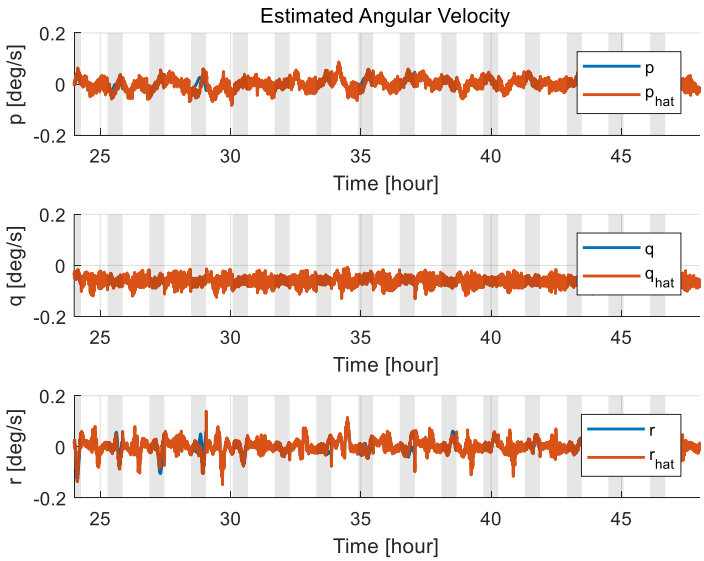

Figure 3.22: Worst Case Simulation Results

– Angular Velocity (Boom Deployed)

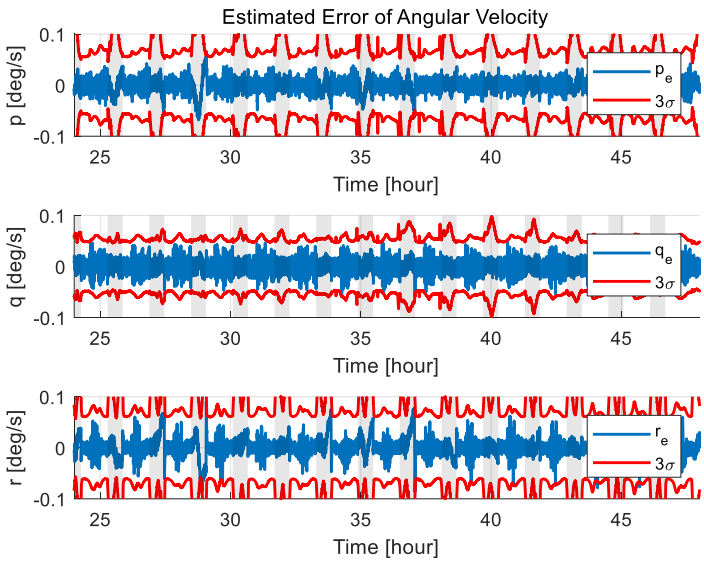

Figure 3.23: Estimation Error

– Angular Velocity (Boom Deployed)

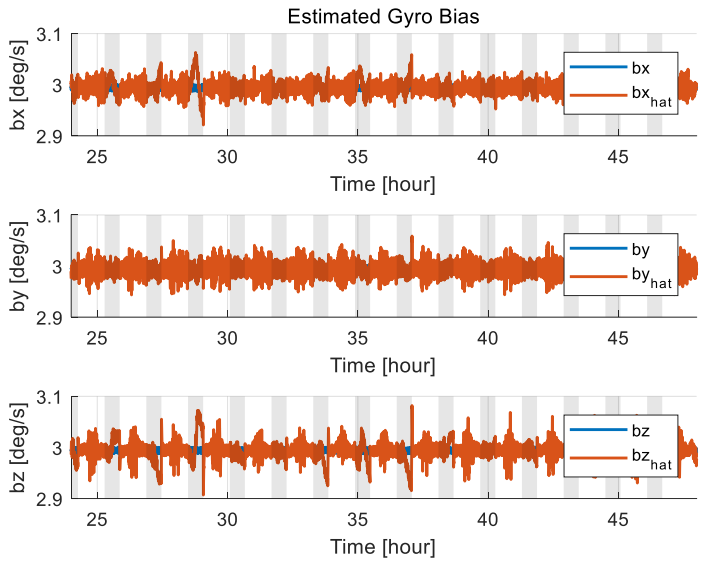

Figure 3.24: Worst Case Simulation Results

– Gyro Bias (Boom Deployed)

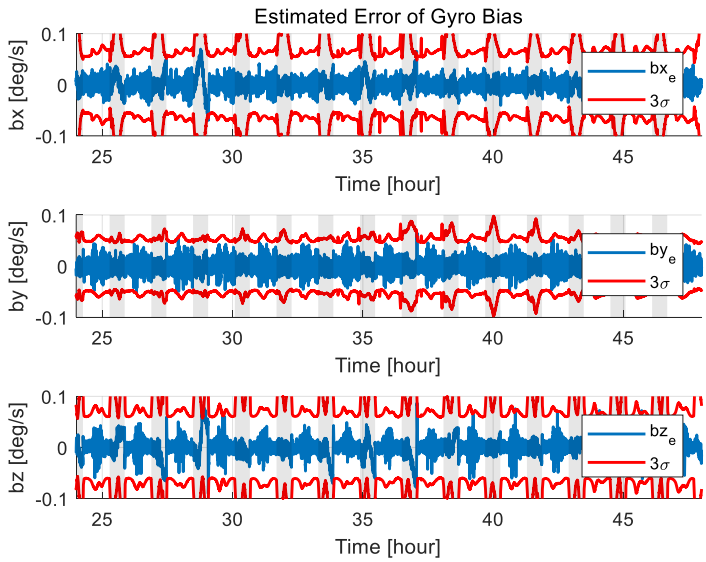

Figure 3.25: Estimation Error

– Gyro Bias (Boom Deployed)

Table 3.11: Control Performances

Mode	RMS		
	ϕ [deg]	θ [deg]	ψ [deg]
Mission Mode (10−24 hours)	9.34	8.52	12.03
Boom Deployed (24−48 hours)	6.83	5.31	11.89

Table 3.12: Estimation Performances – Euler Angle

Mode	RMSE		
	ϕ [deg]	θ [deg]	ψ [deg]
Mission Mode (10−24 hours)	3.20	1.41	4.51
Boom Deployed (24−48 hours)	2.99	1.19	3.99

Table 3.13: Estimation Performances – Angular Velocity

Mode	RMSE		
	p [deg/ s]	q [deg/ s]	r [deg/ s]
Mission Mode (10−24 hours)	0.011	0.011	0.019
Boom Deployed (24−48 hours)	0.012	0.011	0.016

Table 3.14: Estimation Performances – Gyro Bias

Mode	RMSE		
	b_x [deg/ s]	b_y [deg/ s]	b_z [deg/ s]
Mission Mode (10−24 hours)	0.011	0.011	0.019
Boom Deployed (24−48 hours)	0.012	0.011	0.016

The results of SILS including the worst case magnetic field distortion are shown in Figs. 3.14 to 3.25. Figures 3.14 through 3.19 show the results for the mission mode in which the boom is not deployed, and Figures 3.20 through 3.25 show the results for the boom deployed. Performance analysis is summarized in Tables 3.11 to 14.

The overall performance of ADCS performance is not significant when the boom is deployed and when it is not deployed. This is interpreted to be because the air drag and the solar pressure acting when the boom is deployed are smaller than the magnetic field distortions and therefore do not have much effect. The control performance shows that the RMSE of the roll and pitch is less than 10 degrees and the RMSE of the yaw is less than 15 degrees. This is a performance satisfying the above−described requirements. Also, the estimated performance is verified that all results are bounded within 3−sigma of standard deviation. Especially, the attitude is well

estimated even in the sun period where the magnetic field distortion becomes large. This is because we have previously changed the measurement noise according to the magnetic field distortion scenario. The RMSE for angular velocity and gyro bias is very similar, which is confirmed by the sensor noise level.

For the magnetic field distortion performed in this chapter, the dipole moment of the 1st-order Gauss Markov model was applied to each axis. At this time, the distortion level is set at 7% of the maximum output of the magnetorquer. In case of tau, it is set to 10000 so that the magnetic field distortion level changes very slowly. Therefore, it can be said that the magnetic field distortion is greater than the magnetic field distortion in space. And, in a space environment, ADCS performance is expected to be better than simulated performance. Furthermore, PILS was performed in the same way as SILS, and the same results were calculated to verify the program implemented in the OBC.

Chapter 4

Hardware-In-the-Loop Simulation of Attitude Determination and Control System

In this chapter, HILS verification of ADCS using Helmholtz cage is performed. To do this, the mathematical modeling and assembly process of Helmholtz cage is introduced. Then, a desired magnetic field controller generated by Helmholtz cage is designed using a classical control technique. Thereafter, HILS verification of ADCS is performed using the Helmholtz cage. By generating the desired magnetic field in Helmholtz cage, the constraints of the ground environment can be removed and ADCS performance can be verified. To demonstrate the validity of the proposed method, a single axis HILS verification of ADCS using SNUGLITE cube-satellite will be presented.

4.1. Helmholtz Cage Design

4.1.1. Introduction

In previous research of SNUGLITE ADCS, the single-axis ADCS HILS was performed by suspending the cube satellite in the ground environment [16]. However, due to the constraints of the ground environment, ADCS performance verification was limited. In other words, there are problems that are the performance degradations of the estimation and control performances. The estimation performance is degraded due to the magnetic field including the statistical error characteristic, and the control performance is degraded due to the small input torque of the magnetorquer, which is vulnerable to the disturbance. Therefore, in this thesis, HILS verification of ADCS using Helmholtz cage is proposed, focusing on the input torque proportional to the magnitude of the external magnetic field. That is, it overcomes the limitation of existing HILS by controlling the magnetic field vector generated from Helmholtz cage. The proposed HILS is aimed at verifying the performance of ADCS with only the magnetorquer in the ground environment that containing constraints.

Helmholtz coil was proposed by German physicist Hermann von Helmholtz as a device for generating a uniform magnetic field. Helmholtz coils consist of two identical circular coils, with the same

direction and intensity of current flow. If the coil consists of a square coil, it is called Helmholtz cage. In the case of a circular coil, the magnetic field generated at a certain distance from the center has the same magnitude of the magnetic field generated at any point of the circular coil. Therefore, a uniform magnetic field space, where the rate of change of the magnetic field is zero, is generated at the same distance between the radial length of Helmholtz coil and the two coils. However, since Helmholtz coil is a circle shape, it is difficult to make and store. In this thesis, to avoid difficulties of disadvantages of making Helmholtz coil, Helmholtz cage is fabricated with a square coil. Also, a simulation based on mathematical derivation is considered to reduce the nonlinearity and create a uniform magnetic field space of Helmholtz cage.

Another problem with existing HILS is control convergence time. It is a problem solved at the same time as supplementing the small input of the magnetorquer. By making the magnetic field size of Helmholtz cage larger than the geomagnetic field, the convergence time and the disturbance can be reduced. The convergence time according to the magnetic field size can be predicted by simple linear model. If the angular velocity is applied linearly, the following relationship equation is derived.

$$\tau = I \cdot \alpha = \boldsymbol{\mu} \times B, \quad \theta = \frac{1}{2}\alpha t^2 \tag{4.1}$$

$$t = \sqrt{\frac{B}{B_h}} t_0 \tag{4.2}$$

Therefore, the convergence time due to the magnetic field generated by Helmholtz cage is reduced by $\sqrt{B/B_h}$ times. Assuming that the geomagnetic field is constant, a graph of the convergence time is drawn when the magnetic field of the Helmholtz cage is changed. It can be predicted that the convergence time is about 1/2 times when the magnetic field is generated about five times as much as the geomagnetic field.

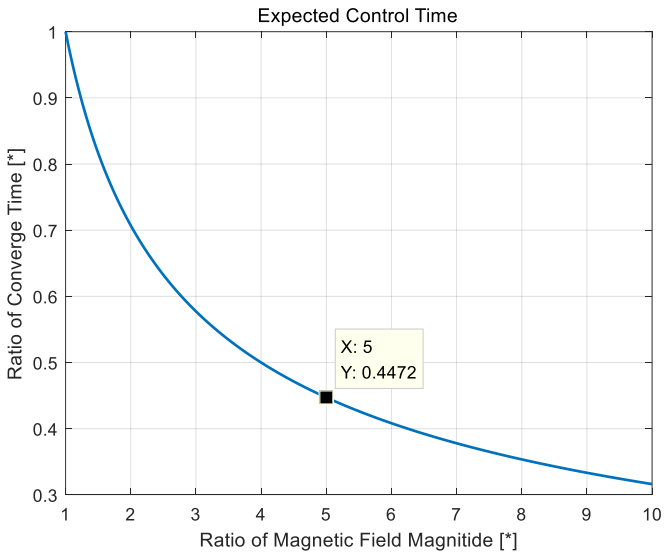

Figure 4.1: Decrease Rate of Convergence Time with Ratio of Magnetic Field Magnitude

Considering all of the above conditions, the design requirements of the Helmholtz cage are selected.

1) All materials consist of non-magnetic materials.
2) A uniform magnetic field covers the cube-satellite 2U size.
3) The maximum magnetic field generated by the Helmholtz cage must be 5 times greater than the geomagnetic field.

The first requirement is to avoid the influence of metallic substances on the magnetic field of Helmholtz cage. For this purpose, it is composed of materials which are not magnetic. The second requirement is that the size of the same magnetic field space should be given, since Helmholtz cage is made up of square wires unlike Helmholtz coils. It should be able to fit the size of cube-satellite. In the case of the final requirement, it can be said that it is a requirement of the HILS presented in this thesis. By generating a large magnetic field, the disturbance can be reduced and the convergence time can be improved.

4.1.2. Mathematical Modeling and Simulation

A mathematical model is derived to simulate the magnetic field generated from Helmholtz cage. All the processes of derivation of the mathematical expressions refer to Gerhardt's work [23].

The equation for the magnetic field is derived based on the Biot-Savart law (Eq. 3.6) [33].

$$B(r_h) = \frac{\mu_0 N}{4\pi} \int \frac{i_h \times \hat{r}_h}{r_h^{\ 2}} dl = \frac{\mu_0 i_h N}{4\pi} \int \frac{dl \times \hat{r}_h}{r_h^{\ 2}} \tag{4.3}$$

The magnetic field spaced by ρ_h from one point on the square wire to one point on the center axis is as follows.

$$dB = \frac{\mu_0 i_h N}{4\pi} \cos\theta d\theta \hat{B} \tag{4.4}$$

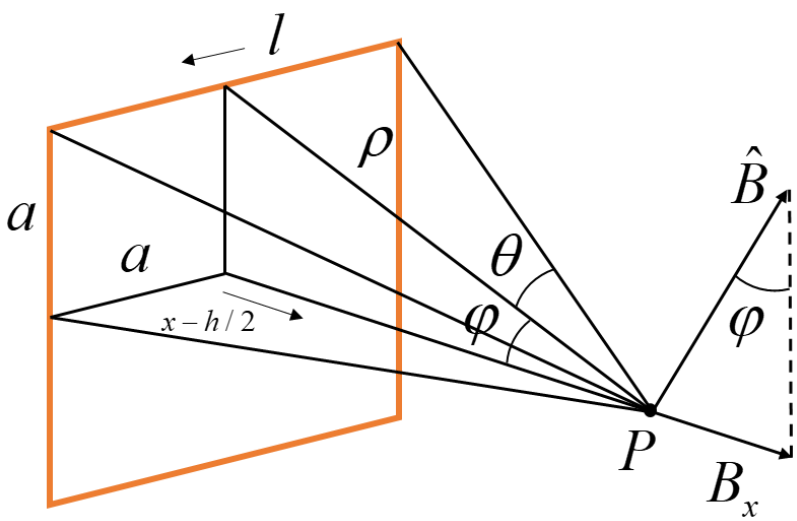

Figure 4.2: Geometry of Single Square Coil

By integrating Equation 4.4, the magnetic field for one side of the square coil can be obtained.

$$B = \int dB = \int_{\theta_1}^{\theta_2} \frac{\mu_0 i_h N}{4\pi} \cos\theta d\theta \hat{B} = \frac{\mu_0 i_h N}{4\pi} \left(\frac{2a}{\sqrt{a^2 + \rho_h{}^2}} \right) \tag{4.5}$$

where,

$$\text{where } \theta_1 = -\sin^{-1}\left(\frac{a}{\sqrt{a^2 + \rho_h{}^2}} \right),\ \theta_2 = \sin^{-1}\left(\frac{a}{\sqrt{a^2 + \rho_h{}^2}} \right)$$

By summing the magnetic fields for the four conductors, the formula for the magnetic field at one point (P) of the central axis of the square conductor is summarized.

$$B_s(x) = 4B\sin\phi = \frac{\mu_0 i_h}{\pi} \frac{2a^2}{\left(a^2 + x^2\right)\left(2a^2 + x^2\right)^{\frac{1}{2}}} \tag{4.6}$$

Since the Helmholtz cage is made up of two square coils, the sum of the magnetic fields of the coils must be obtained. The magnetic field for the square coils spaced by $h/2$ relative to the reference point x passing through the central axis is derived as follows.

$$B_h(x) = \frac{\mu_0 i_h N}{\pi} \left[\frac{2a^2}{\left(a^2 + (x - h/2)^2\right)\left(2a^2 + (x - h/2)^2\right)^{\frac{1}{2}}} + \frac{2a^2}{\left(a^2 + (x + h/2)^2\right)\left(2a^2 + (x + h/2)^2\right)^{\frac{1}{2}}} \right] \tag{4.7}$$

Based on the derived formula, the magnetic field generated in the Helmholtz cage can be simulated according to the position on the central axis. In order to check the nonlinearity of the magnetic field, the simulation result is shown in the Figure 4.4. Since the nonlinearity depends on the distance between the square coils, the results for the half of length (a) and the distance (h) between the coils are shown.

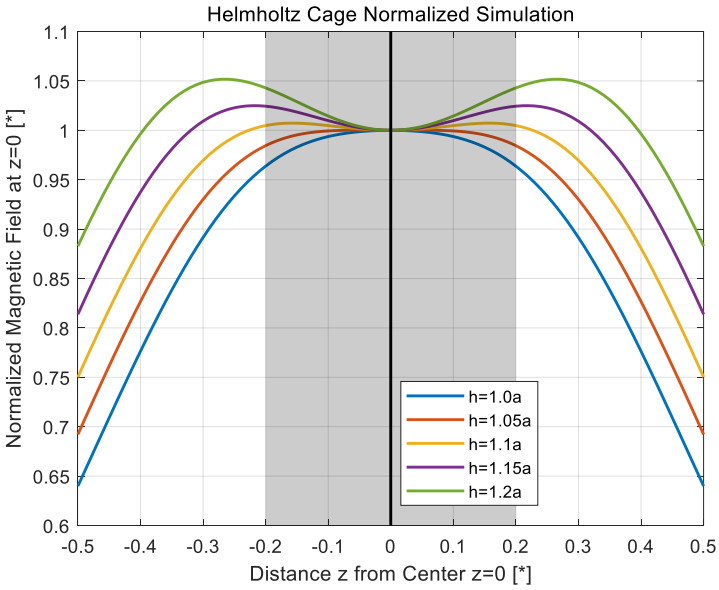

Figure 4.3: Normalized Simulation of Helmholtz Cage

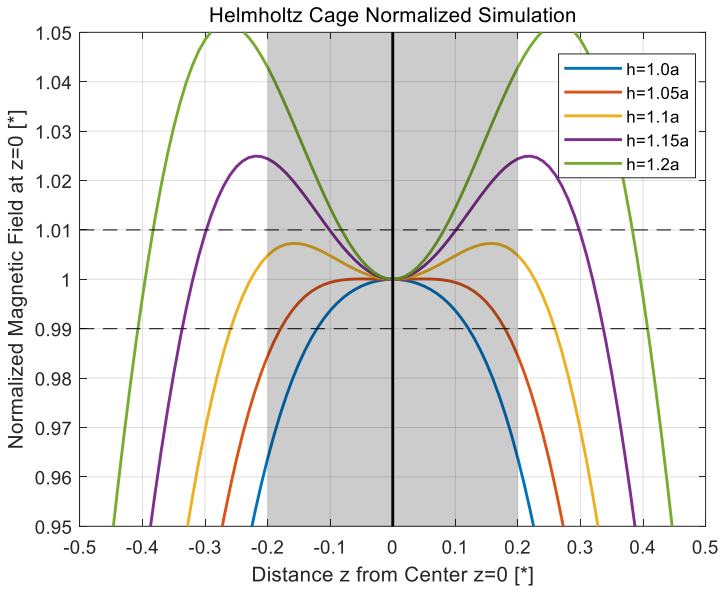

Figure 4.4: Normalized Simulation of Helmholtz Cage for Nonlinearity (1%)

The uniform magnetic field is set to 2/5 of the length of the distance (h) and is the same as the area marked in black on the graph. In the case of nonlinearity, it is confirmed that the error rate of the magnetic field is less than 1% when $h = 1.1a$. Therefore, the relation between the distance between the coils and the length of the square wire is set to $h = 1.1a$. Thereafter, a uniform space length of $40cm$ is set by setting $a = 0.6m$ for the space where the cube-satellite will be sufficiently covered. This is a volume of $40cm^3$ in three dimensions.

4.1.3. CAD and Assembly

Consider the given h as the z-axis located at the innermost position of Helmholtz cage. Then, 3-axis Helmholtz cage is designed by constructing additional x and y axes square coils outside it. To design the Helmholtz cage, Computer-Aided-Design (CAD) is used first. The U-shaped aluminum frame as shown in the following figure is used for the material of one side of the square coil which is used basically. Aluminum is not only magnetic, but also inexpensive, so it can be easily machined and assembled.

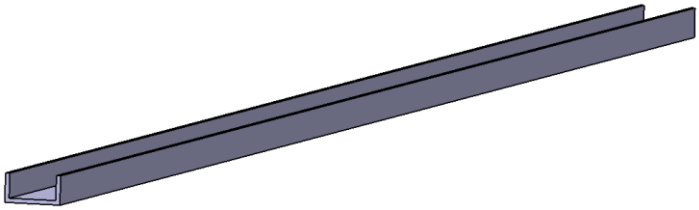

Figure 4.5: U-shaped Aluminum Frame

In addition, the connections connecting the frames are made using 3D printer output. 3D printer printouts are plastic materials that are easy to make, hard, and non-magnetic. Using this, one basic square coil can be created as shown in the following figure.

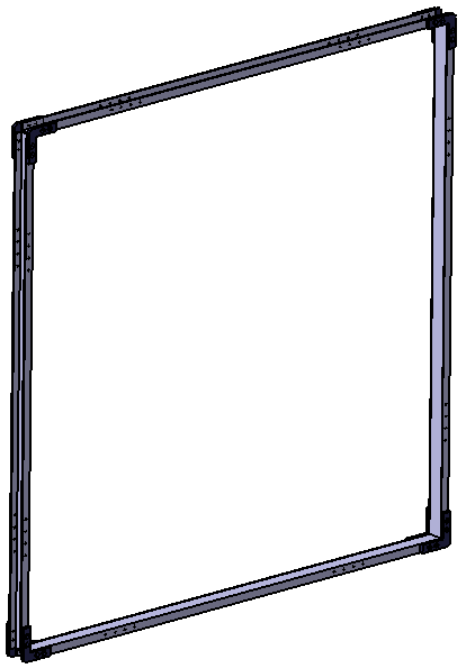

Figure 4.6: A Square Coil Made of
the U-shaped Aluminum Frame

Finally, 3-axis Helmholtz cage is constructed as shown in the following figure. Here, the middle box is a $40cm^3$ space with a uniform magnetic field, and a reference sensor fixture was prepared to feed back the measurement of magnetic field generated by the Helmholtz cage. In addition, the bolts and nuts also use titanium materials to remove the metallicity.

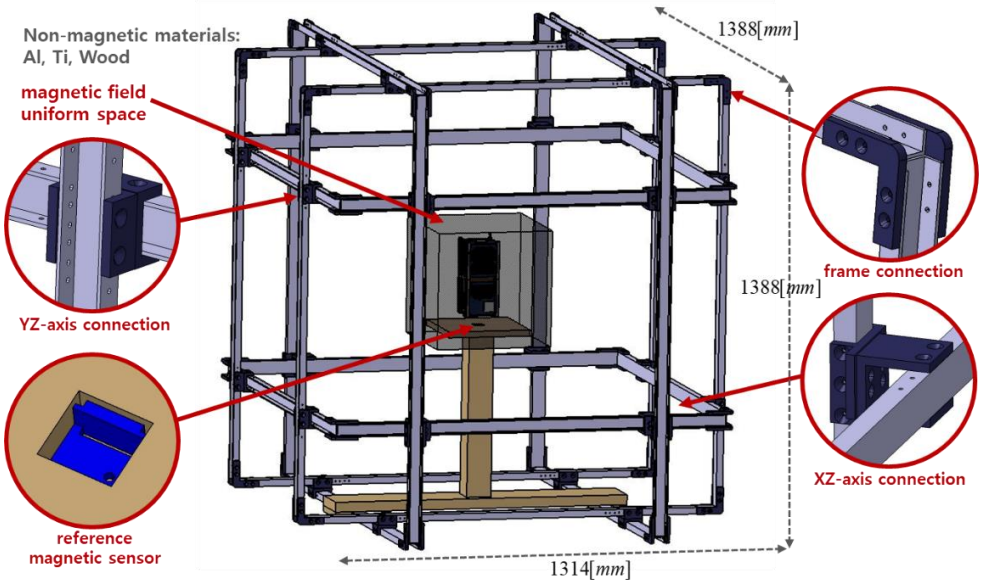

Figure 4.7: Helmholtz Cage CAD Model

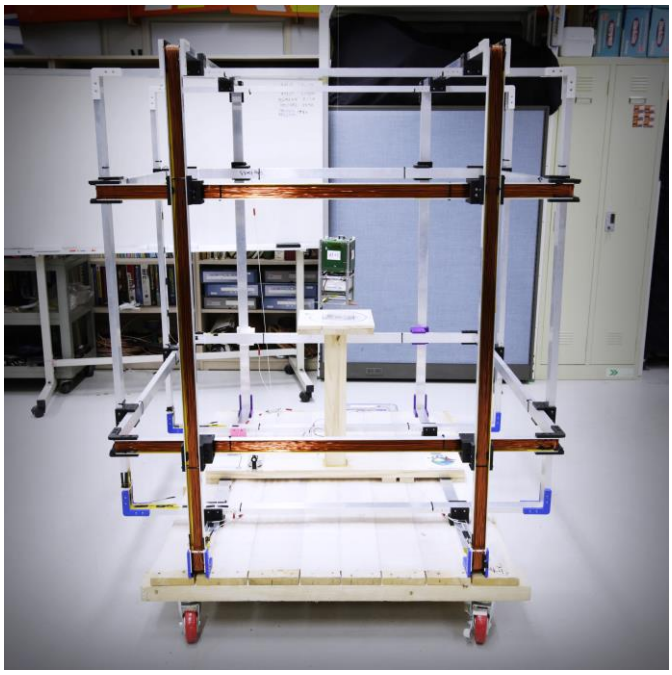

Figure 4.8: Assembled Helmholtz Cage

Table 4.1: Helmholtz Cage Size Specifications

Size	$1314 \times 1388 \times 1388\ [mm^3]$
x−axis length (a_x)	674 $[mm]$
y−axis length (a_x)	637 $[mm]$
z−axis length (a_x)	600 $[mm]$
x−axis distance (h_x)	760 $[mm]$
y−axis distance (h_y)	720 $[mm]$
z−axis distance (h_z)	678 $[mm]$
Materials	Aluminum, Wood, Plastic, Titanium

4.1.4. Driving Circuit Design

An electronic circuit for generating a magnetic field in a given Helmholtz cage frame is constructed. First, a coil for generating a magnetic field is selected. The enamel wire is used as the material of the coil, and the coil, which can generate up to 10 times of the geomagnetic field, is designed by using the simulation. This is a condition that satisfies the requirement. The selected enamel wire and the simulation for each axis are composed as follows. A resistor is added to properly adjust the generated magnetic field.

Table 4.2: Specification for Magnetic Field Generation

Axis	Voltage [V]	Maximum Current [A]	Wire Diameter [mm]	Number of Turns	Maximum Magnetic Field [$mGauss$]
X	24	3.84	1.40	45	2047
Y	24	3.65	1.30	45	2056
Z	24	3.46	1.20	45	2070

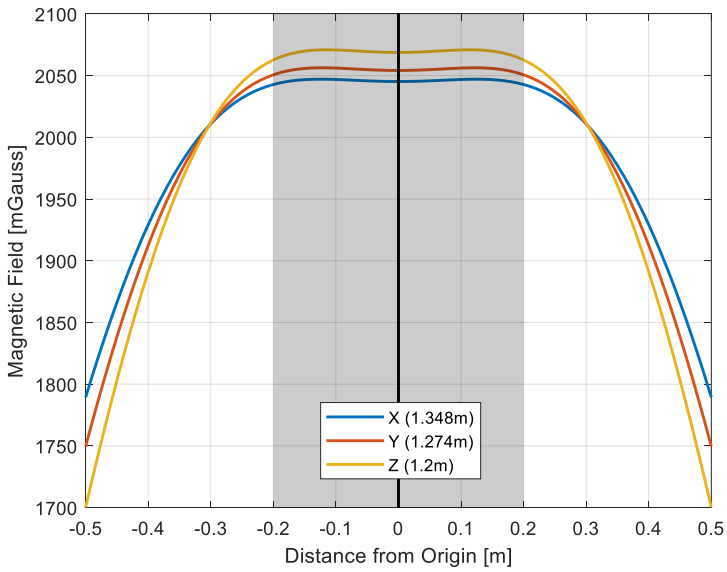

Figure 4.9: Simulation Results of Maximum Magnetic field Generated in Helmholtz cage

Bi-directional driving of the magnetic field and size-adjustable circuit are designed using the configured enamel wire. The magnetic field is adjustable by Pulse Width Modulation (PWM) duty and Microcomputer (MCU) is used for real time control. The devices used are as shown in the following table.

Table 4.3: Elements used in Helmholtz Cage Driving Circuit

Part	Part Name	Quantity
Microcontroller	Atmega128	1
24 Voltage Power Supply	UP100S24	3
12 Voltage Power Supply	US75S12	1
High Side Switch	BTS442E2	3
PWM Switching Driver	DCMD-100-D-OD	6
Relay	JS1a-5V	6
Magnetometer	Honeywell HMC5883L	1
Temperature Sensor	Invensence ITG-3200	1

There are three main parts of the Helmholtz cage: Control Software, Direction Circuit, and Hardware.

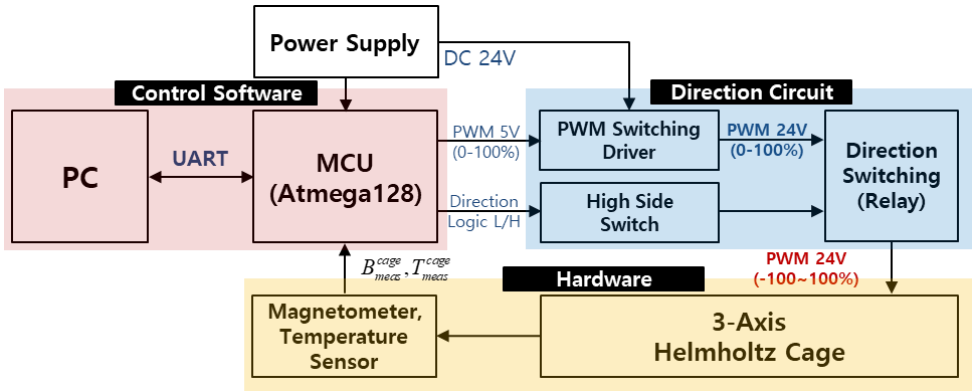

Figure 4.10: Overall Block Diagram of Helmholtz Cage System – the sampling frequency of the system is 50[Hz]

The Control Software part controls the magnetic field in real time, and the magnetic field controller is implemented. MCU drives the magnetic field with PWM and can command the direction change through direction logic. In the direction circuit part, voltage boosting is performed with the relay element for changing direction. PWM provided by the MCU is TTL level, but in this part, it is boosted to the voltage supplied by the power supply. The hardware part is where the magnetic field is generated and the magnetic field is measured. The magnetometer is temperature compensated in the same way as in Chapter 3.

4.1.5. Magnetic Field Controller Design

A classical control technique is used to design the controller of a given Helmholtz cage. First, the transfer function is derived from the mathematical modeling of Helmholtz coils. From Equation 4.7, since the magnetometer is fixed at the center of Helmholtz cage, other constants except the current can be treated as constants. Therefore, Equation 4.7 can be simplified as follows. The electrical time lag, etc., occurring in the circuit is ignored.

$$B_h(t) = K_h \cdot i_h(t) \tag{4.8}$$

A simple constant gain transfer function can be obtained by Laplace transform. Since the PWM duty is controlled in the configured drive circuit, it can be written in terms of voltage.

$$B_h(s) = K_h \cdot i_h(s) = \frac{K_h}{R} V(s) \tag{4.9}$$

$$G_h(s) = \frac{B_h(s)}{V(s)} = K_{h'} \ \frac{[mGauss]}{[V]} \tag{4.10}$$

here,

$$\begin{aligned} K_{h'} &= [K_{h'}^{x} \quad K_{h'}^{y} \quad K_{h'}^{z}] \\ &= \begin{bmatrix} 21.69 & 23.50 & 21.29 \end{bmatrix} \end{aligned}$$

In order to design a controller using a given equation, the structure of the controller must be determined. Since it is a simple constant transfer function, the I-controller structure is adopted. Because SNUGLITE ADCS is a very slow system and the transfer function of Helmholtz cage is similar to that of the P-controller, it is the same as the PI controller. If a PID-controller is adopted, a faster rising time can be achieved, but the D-controller is not suitable for the stability of Helmholtz cage requiring high currents, and its implementation becomes complicated. Therefore, only the I controller is adopted, and the controller is designed easily by using the pole-placement technique. The requirements of the controller design are selected so that stability is given priority. Phase Margin

(PM) and Gain Margin (GM) should be more than 40 degrees, respectively. Since the system is slow, the rising time (0−90%) should be within 1 second.

A classically controlled pole−placement technique is used for controller design [34]. The transfer function of the I−controller is defined as follows.

$$G_c(s) = \frac{K_i}{s} \tag{4.11}$$

Therefore, the transfer function for the closed loop is simply summarized.

$$G_{cl}(s) = \frac{K_i K_{h'}}{s + K_i K_{h'}} \triangleq \frac{\alpha}{s + \alpha} \tag{4.12}$$

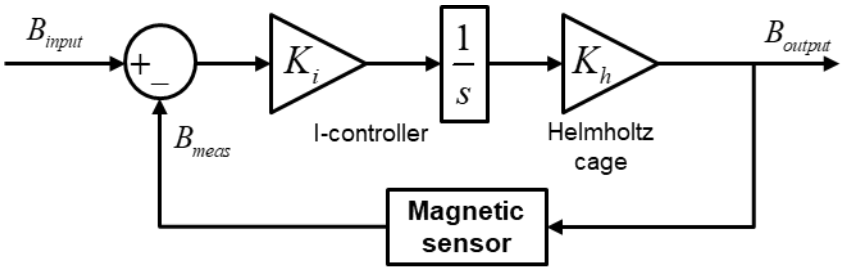

Figure 4.11: Block diagram of Helmholtz Cage Magnetic Field Controller

Pole placement techniques for controller design are now applied. If the pole of the system (α) is designed to be larger than the sampling

frequency (f_{sys}) of the system, the gain of the controller is calculated. This is because the pole does not affect the system. In this thesis, the controller frequency is set to three times.

$$\alpha = K_i K_h = 2\pi \frac{f_{sys}}{3},\ K_i = \frac{\alpha}{K_h} \tag{4.13}$$

here,

$$\begin{aligned} K_i &= \begin{bmatrix} K_i^x & K_i^y & K_i^z \end{bmatrix} \\ &= \begin{bmatrix} 4.34 & 4.01 & 4.43 \end{bmatrix} \end{aligned}$$

To verify that the performance of the designed controller satisfies the requirements, performance was verified through initial simulation.

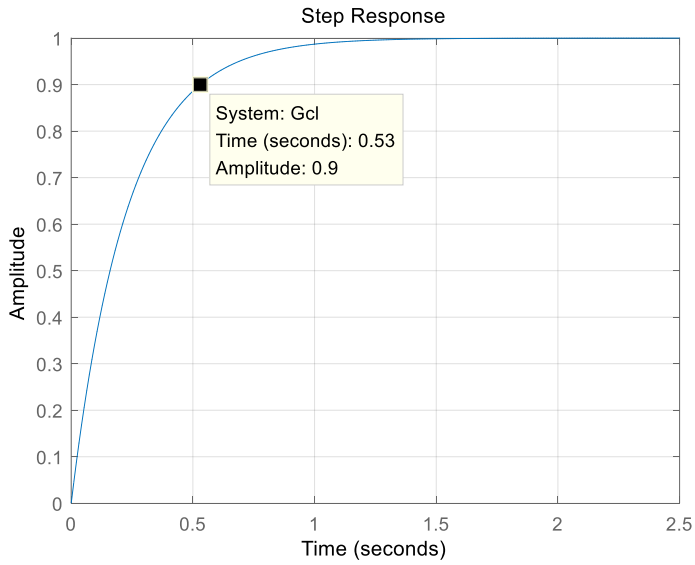

Figure 4.12: Step Response of Closed Loop

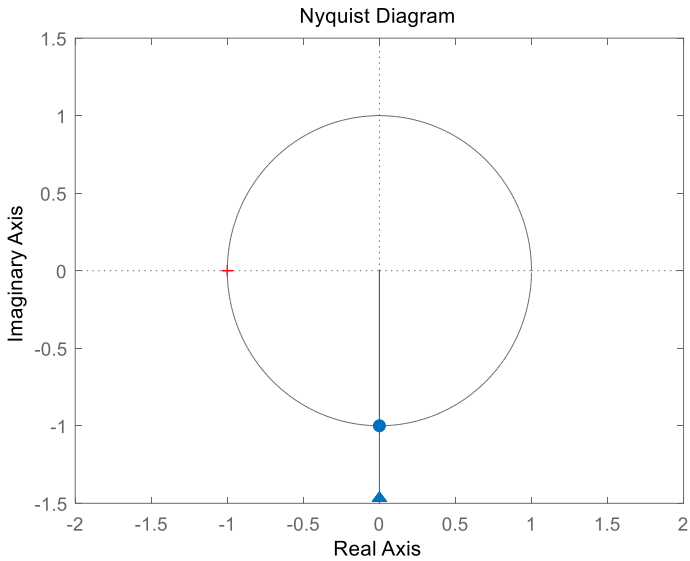

Figure 4.13: Nyquist Diagram

Through the simulation, it is confirmed that the designed controller satisfies the requirement. In the step response plot, it is confirmed that the rising time (0−90%) is 0.53 seconds, converging within 1 second. In addition, it is proved that the transfer function model is consist of a first−order integrator, and that GM has stability for infinity and PM has 90−degree margin stability.

Now, through actual implementation, controller performance is verified. The integrator is implemented using Tustin's method. The experiment result of $1000\,[mGauss]$ step input is shown in the following figure. Here, the initial value of each axis is offset, which is an indoor magnetic field measurement.

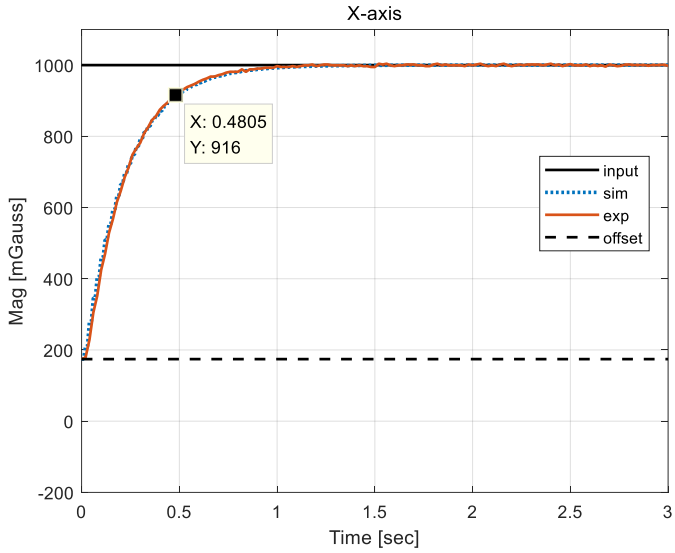

Figure 4.14: Experiment Result – Step Response

when Input is $B_{input}^{x} = 1000\ [mGauss]$

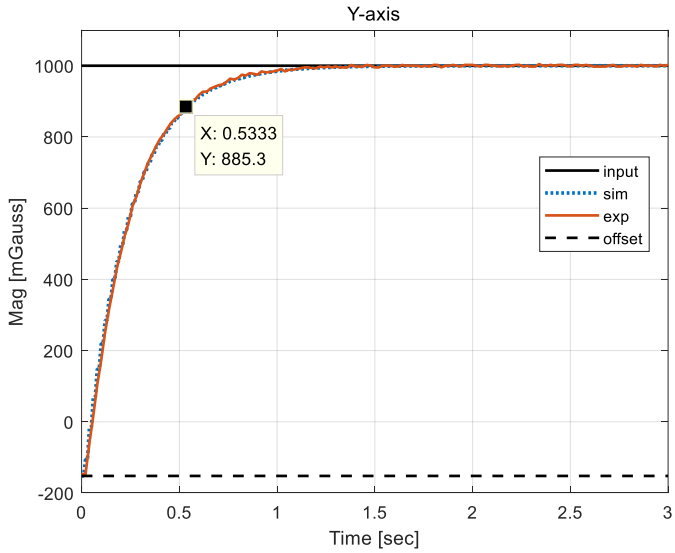

Figure 4.15: Experiment Result – Step Response

when Input is $B_{input}^{y} = 1000\ [mGauss]$

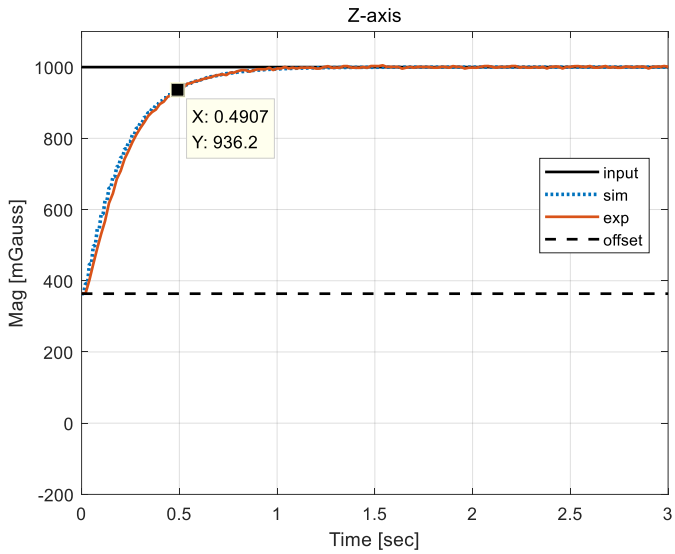

Figure 4.16: Experiment Result – Step Response

when Input is $B_{input}^{y} = 1000\ [mGauss]$

Experiment results show that the rising time (0–90%) is 0.49, 0.53, and 0.49 seconds, respectively. Now, based on the designed Helmholtz cage, a HILS environment will be constructed and experiments will be conducted.

4.2. Hardware-In-the-Loop-Simulation

4.2.1. HILS Configuration

The Helmholtz coils equipped with the designed controller are used to construct a complemented HILS. The constructed HILS environment hangs SNUGLITE EM on the room and simulates the sun

using a halogen lamp [13]. And, the magnetic field generated by the Helmholtz cage is used. This magnetic field is generated five times as much as the xy-plane geomagnetic field for degrading external force of HILS. This is a size that can reduce convergence time by half. Then, GPS measurements cannot be calculated in the established experimental environment. Therefore, as shown in the following figure, the nadir-pointing attitude is simulated by redefining the mean measurements of the simulated sunlight and the magnetic field as a reference vector.

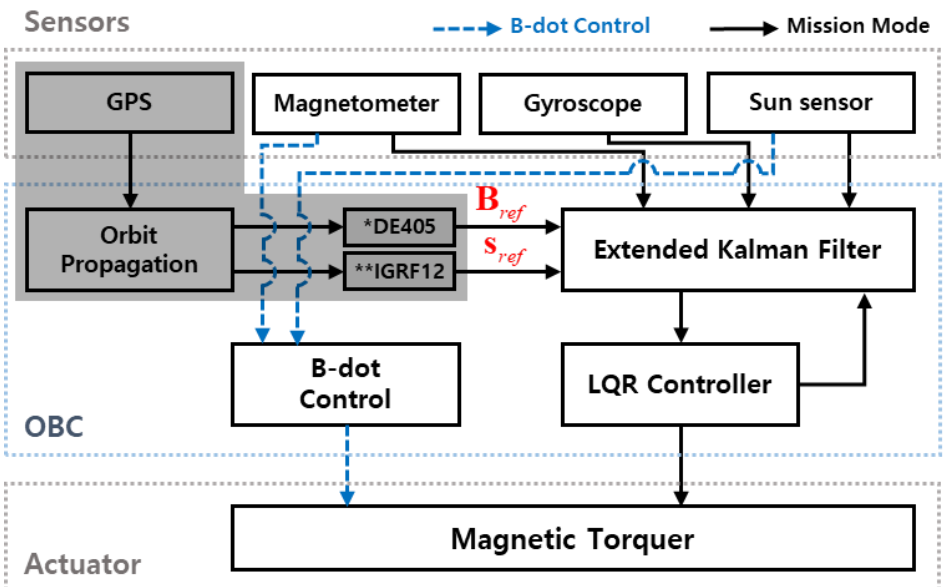

Figure 4.17: Overall System of SNUGLITE ADCS in the Ground Environment

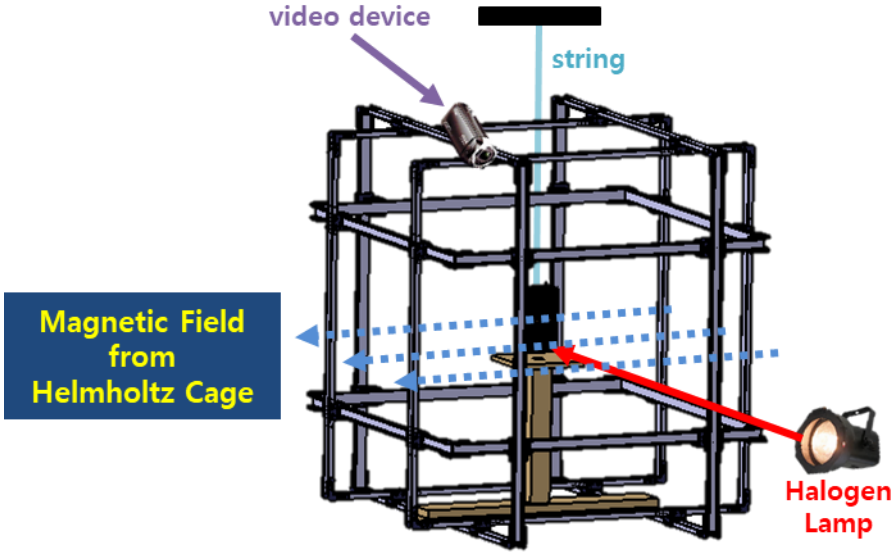

Figure 4.18: Proposed HILS Configuration

Using Helmholtz Cage

Figure 4.19: Implemented HILS Configuration

The external force of the proposed HILS environment and the space environment can be compared by dividing the gravity gradient torque and the string torque. First, the worst case gravity is calculated when $\theta = 45^{\circ}$.

$$\begin{aligned}\tau_{gg}^{\max} &= \frac{3\mu_e}{2R_e^{\,3}}\left|I_x - I_z\right|\sin 2\theta \\ &= \frac{3\times\left(3.986\times10^5[km^3/s^2]\right)\times(0.0054-0.0022[kg\cdot m^2])(\sin(2\times45^{\circ}))}{2\times(6.9781\times10^3[km])} \\ &= 5.68\times10^{-9}\,[N\cdot m]\end{aligned} \tag{4.14}$$

Second, the external force in the ground environment is calculated as a torsional pendulum model [13] [35]. Since the string torque is proportional to the angle of rotation, it is assumed that the external force is maximum when rotated 180 degrees. Here, the torsional constant (κ) can be obtained by the period of the torsional pendulum.

$$\begin{aligned}\tau_{str}^{\max} &= \kappa\theta \\ &= 5.76\times10^{-8}[N\cdot m/rad]\times\pi[rad] \\ &= 1.81\times10^{-7}[N\cdot m]\end{aligned} \tag{4.15}$$

Since the maximum dipole moment output of the magnetorquer of SNUGLITE is $0.038\,[A\cdot m^2]$, the maximum input torque is calculated as following Equation. The magnetic field calculated by the cross product is the average magnetic field size in space. This is similar to the size of the xy−plane magnetic field in the ground environment.

$$
\begin{aligned}
\tau_{mt}^{\max} &= \boldsymbol{\mu}_{\max} \times \mathbf{B} \\
&= 0.038[A \cdot m^2] \times (2.5 \times 10^{-5}[T]) \\
&= 9.5 \times 10^{-7}[N \cdot m]
\end{aligned} \tag{4.16}
$$

The comparison results for each environment, including the calculated external forces, are shown in Table 4.4. In the case of space environment, Gravity gradient torque is the most dominant torque. Therefore, only the gravitational gradient torque is considered as an external force. Since the gravity gradient torque is less than 1% of the maximum magnetorquer input torque, it can be considered that the external force is insufficient in a space environment. However, in the existing HILS environment, the string torque is 20% of the maximum input torque. For this reason, HILS verification of ADCS with magnetorquer is very difficult. In other words, to successfully perform a HILS, it is always necessary to have a torque of more than 20% of the maximum torque input. To solve this problem, a magnetic field is generated in the Helmholtz cage to increase the input torque. As a result, in the proposed HILS environment, the external force is reduced to 5% of the maximum input torque when the magnetic field generated from Helmholtz cage is 5 times bigger than before.

Table 4.4: Comparison of HILS and Space Environment

Environment	Max. External Torque ($\tau_{ext}^{\max}$)	$\tau_{ext}^{\max} / \tau_{mt}^{\max}$	Magnetic Field	Reference Vector
Space	$\tau_{gg}^{\max}$	$<1\%$	$\mathbf{B}$	IGRF12, DE405
Existing HILS	$\tau_{str}^{\max} + \varepsilon$	$\approx 20\%$	$\mathbf{B} + \mathbf{B}_{build}$	Average Measurement
Proposed HILS		$\approx 5\%$	$\mathbf{B}_h = 5 \times \mathbf{B}$	

Next, in order to HILS in the proposed environment, a single axis control simulation is considered. By defining a coordinate system based on the Helmholtz cage in the proposed HILS environment, a simulation of the nadir-pointing control in the ground environment can be constructed.

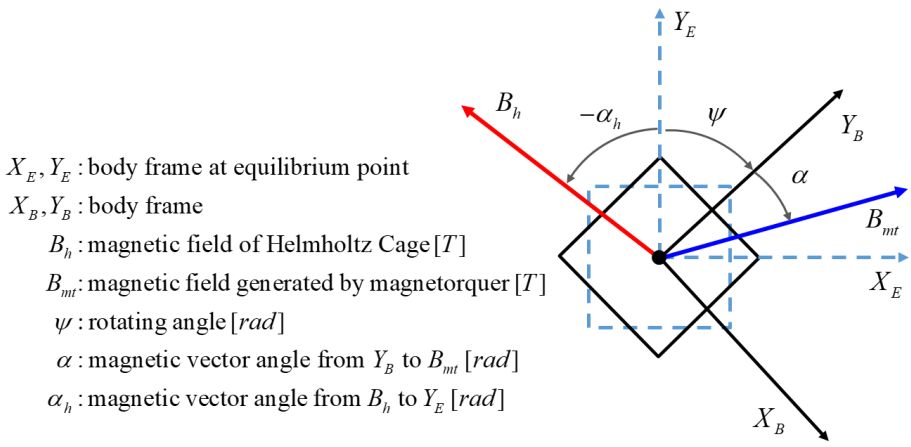

Figure 4.20: A Coordinate System of Proposed HILS Environment

There are two kinds of coordinate systems that are composed in the simulation. Body frame, and equilibrium frame. The coordinate system for the equilibrium frame is based on the equilibrium point of the torsional pendulum. In addition, there are two magnetic field vectors. The magnetic field vector of the Helmholtz cage and the input vector generated by the magnetorquer. The reason is that two magnetic field vectors are considered because the cube-satellite attitude changes due to the interference of the magnetic field vectors. Therefore, the single-axis attitude model is derived by the following Equation 4.17. The attitude is determined by the string torque and the input torque of the magnetorquer.

$$I_z\ddot{\psi} + \kappa\psi = \boldsymbol{\mu} \times \mathbf{B}_h \tag{4.17}$$

$$\begin{aligned} B_x(t) &= \|\mathbf{B}_h\| \sin(\psi(t) + \alpha_h) \\ B_y(t) &= \|\mathbf{B}_h\| \cos(\psi(t) + \alpha_h) \end{aligned} \tag{4.18}$$

here, the magnetic field measured in the body according to the attitude is derived as Equation 4.18.

Based on this simulation, the performance of the proposed ADCS can be analyzed by comparison with actual experimental results. In the case of simulation, the attitude information does not include the estimation algorithm. Therefore, assuming that the attitude information of the simulation is true value, the estimation and the control performance are analyzed together by comparing the experimental results.

However, if a single-axis control experiment is performed through the proposed simulation, it is impossible to verify ADCS on the ground with the weight of the controller set Q_c, R_c in the space environment. In a space environment, the weight of the Q_c, R_c matrixes for the Ricci algebraic equation of Equation 2.53 is set as following Equation 4.19. This is because gravity gradient torque in space is an external force that helps stabilize the attitude. The force is applied to the largest moment of inertia of the 2U cube-satellite, and it is applied to help the maintaining nadir-pointing with oscillations. Further, since the gravity gradient torque is indecipherable, it is sufficient to maintain the nadir-pointing attitude by the input torque. On the other hand, on the ground, string torque does not help the nadir-pointing, that returns to the equilibrium point of torsional pendulum. In general, the equilibrium point of a torsional pendulum is difficult to find, and string torque is very small and constantly changes due to external conditions such as elasticity and temperature. Therefore, in order to maintain the simulated nadir-pointing in the ground experiment, the input torque must sufficiently overcome the external force of string. For this reason, we conclude from the simulation results that the weights set in the space environment are not appropriate for the ground environment HILS.

In the case of ground HILS, LQR weighting matrixes Q_c, R_c for single axis control are introduced for the verification of the algorithm. The state variable of LQR controller of Equation 2.49 is rewritten as follows.

$$\mathbf{x}_c = \begin{bmatrix} \phi & p & \theta & \delta q & \psi & r \end{bmatrix}^T, \ \mathbf{u} = \boldsymbol{\mu} = \begin{bmatrix} \mu_x & \mu_y & \mu_z \end{bmatrix}^T \tag{4.19}$$

For this state variable, the control weights for the space environment and the ground environment are set to minimize the following cost function.

$$J = \frac{1}{2}\int_0^\infty \left[\mathbf{x}_c{}^T A \mathbf{x}_c + \rho \mathbf{u}_c{}^T B \mathbf{u}_c \right] dt \tag{4.20}$$

here, constant ρ is introduced to take into account relationship between the system state and the input state.

The control weight of the space environment is given by Equation 4.21. For this reason, the roll and pitch angles are set to 5 degrees, the angular velocity is 0.04 degree per seconds, and yaw is set to twice the roll and pitch tolerance. Input state weight is 100% dipole moment, and rho is interpreted as 1% input when in steady−state state.

$$Q_c = diag\left[\left(\frac{1}{5}\right)^2 \ \left(\frac{1}{0.04}\right)^2 \ \left(\frac{1}{5}\right)^2 \ \left(\frac{1}{0.04}\right)^2 \ \left(\frac{1}{10}\right)^2 \ \left(\frac{1}{0.08}\right)^2 \right] in\left[\frac{1}{(\mathrm{deg})^2}\right], \left[\frac{1}{(\mathrm{deg}/s)^2}\right]$$

$$R_c = 100^2 \times diag\left[\left(\frac{1}{0.038}\right)^2 \ \left(\frac{1}{0.038}\right)^2 \ \left(\frac{1}{0.038}\right)^2 \right] in\left[\frac{1}{(A \cdot m^2)^2}\right] \tag{4.21}$$

In contrast, the control weight of the ground environment HILS is given by Equation 4.22 below. Since it is a single axis attitude control HILS, yaw is firstly weighted. The tolerance for yaw axis state was designed at an angle of 10 degrees and an angular velocity of 0.5 degree per seconds. Unlike the space environment, the allowable value of the angular velocity is set to a large value because the input and the external torque are larger than the space environment. Also, the weight of the roll and pitch is given as 20 times the value of yaw so that it can be ignored. The input is 100% dipole moment, and ρ is to increase the input torque to prevent disturbance.

$$Q_c = diag\left[\left(\frac{1}{100}\right)^2 \quad \left(\frac{1}{5}\right)^2 \quad \left(\frac{1}{100}\right)^2 \quad \left(\frac{1}{5}\right)^2 \quad \left(\frac{1}{10}\right)^2 \quad \left(\frac{1}{0.5}\right)^2\right] in\left[\frac{1}{(\mathrm{deg})^2}\right],\left[\frac{1}{(\mathrm{deg}/s)^2}\right]$$
$$R_c = 0.7^2 \times diag\left[\left(\frac{1}{0.038}\right)^2 \quad \left(\frac{1}{0.038}\right)^2 \quad \left(\frac{1}{0.038}\right)^2\right] in\left[\frac{1}{(A\cdot m^2)^2}\right]$$

(4.22)

The simulation results show that the controllers tuned to the space environment and the ground environment are shown in the following figure.

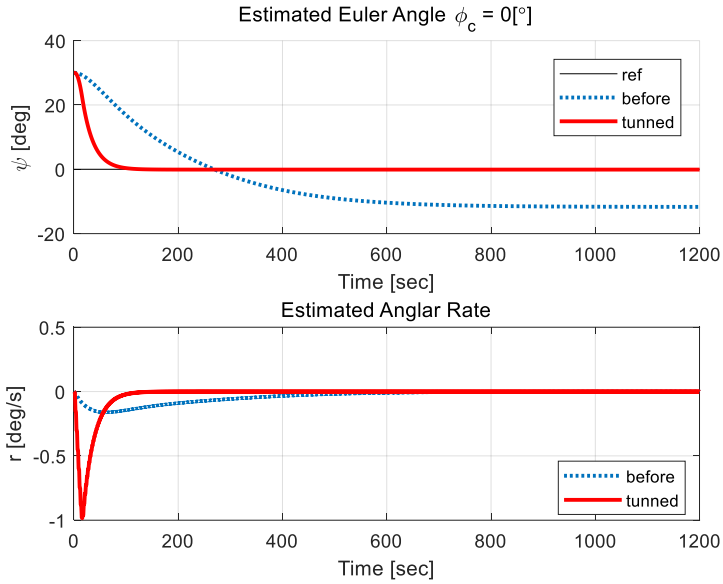

Figure 4.21: Simulation Result for HILS – Comparing LQR Controller Weighing Cases

In the case of space environment weights, steady-state error is occurred, but the controller weights of the ground environment are confirmed to reduce the steady-state error. Thus, by applying the designed weights, single axis attitude determination and control HILS will be performed.

4.2.2. Experiment Results

The results of the comparison between the proposed HILS and the existing HILS in the same environment are shown in the following figure.

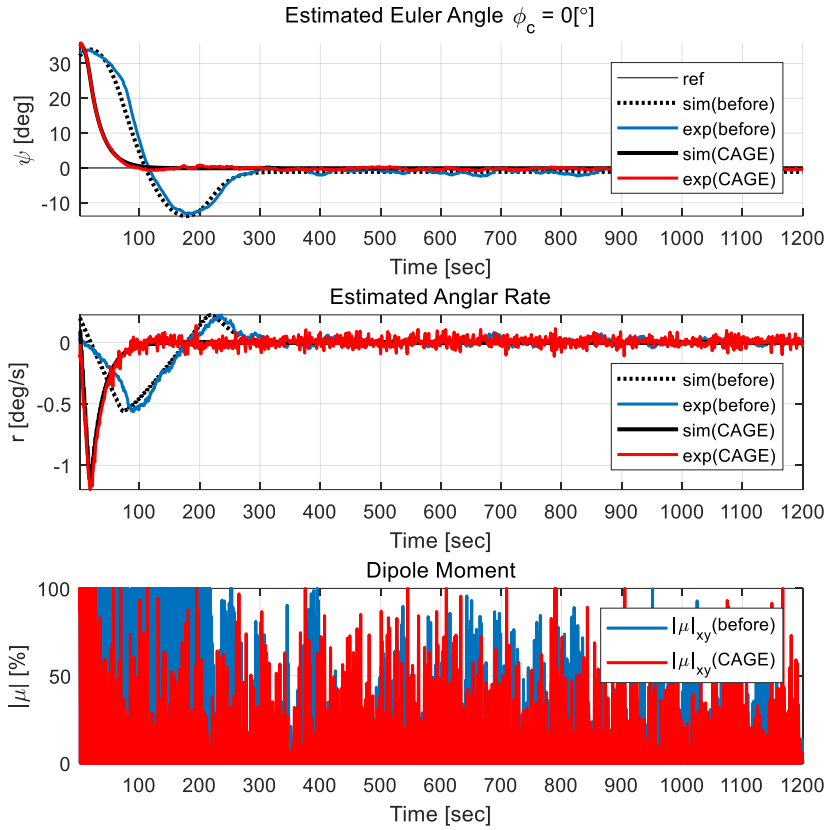

Figure 4.22: Experimental Results of

Single-axis ADCS HILS

As shown in the figure, the existing HILS method has an error with simulation. This is because disturbance factors not considered in the simulation affect the estimation and control performance. Also, even in the steady-state, an error exists around the control input of 0 degree. In addition, the dipole moment is confirmed to be continuously used 100% of the input within the initial 300 seconds.

In contrast, the proposed HILS results using Helmholtz cage are consistent with simulation and experimental results. This is because the error element is removed from the Helmholtz cage by controlling the magnetic field. The dipole moment results also confirm that less saturation occurs.

In order to compare and analyze the experimental results, the result of enlarging the graph for Euler angles is shown in the following figure.

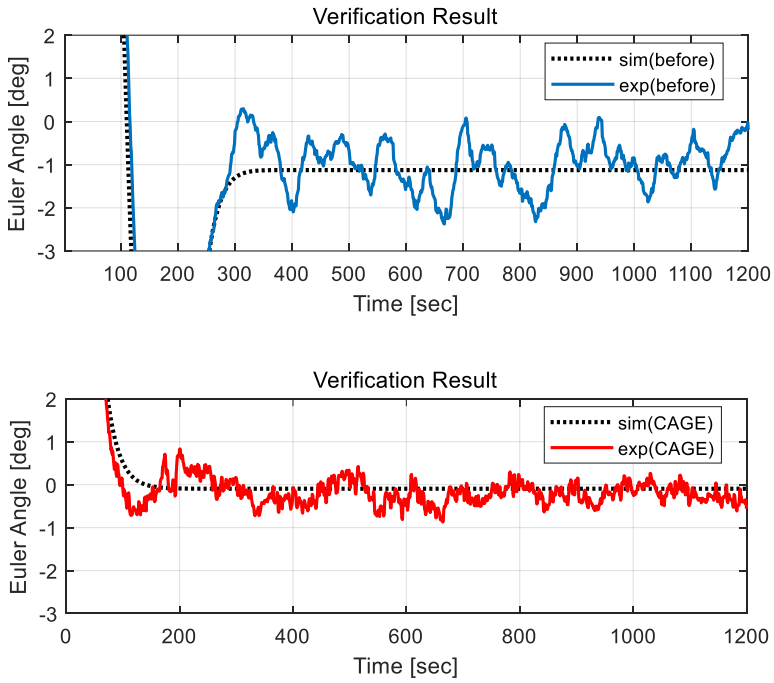

Figure 4.23: Expanded Experimental Results

The results of the analysis are shown in the following tables.

Table 4.5: Converge Time

–	Before	Proposed	Improvement
Time	350 [sec]	184 [sec]	47%

Table 4.6: Steady-State Error (400-1200 seconds)

Error	Before	Proposed	Improvement
RMS	1.17°	0.32°	72%
Max	2.38°	0.87°	63%

Table 4.7: Control Input (Dipole Moment, $\mu_{\max} = 0.038[A \cdot m^2]$)

Time	Before	Proposed	Improvement
~100 seconds	98.3%	64.2%	35%
Steady-state	44.5%	41.7%	6%

First, in convergence time, convergence time is reduced to about half when the magnetic field is generated at 5 times the earth magnetic field as expected in Fig. 4.1. When the errors between 400 and 1200 seconds were defined as steady-state, the RMS values of Euler angle were 1.17 and 0.32 degrees, respectively, and the maximum values were 2.38 and 0.87, respectively, showing a performance improvement of 72% and 63%. In the case of the magnetorquer input, the input approaching the saturation of RMS 98.3%

was consumed in the existing HILS up to the initial 100 seconds, whereas the proposed method showed a performance improvement of 35% by using the input of 64.2%. In steady−state, the performance was improved by 6% from 44.5% to 41.1%. As a result, the proposed HILS was verified through experiments for ADCS equipped with only magnetoquer, and the limit of the ground experiment was overcome by using the Helmholtz cage.

Chapter 5
Conclusion

In this thesis, HILS using Helmholtz cage for low-earth orbit cube-satellite Attitude Determination and Control System (ADCS) verification has been proposed. The proposed method reduced the constraint that occurs in the ground environment HILS by using Helmholtz cage. Through this, it was shown that it is possible to verify the attitude determination and control system for maintaining the nadir-pointing using only the magnetorquer. In order to effectively handle this HILS verification of ADCS, two approaches have been suggested.

First, an algorithm to compensate the magnetic field distortion of the cube-satellite ADCS has been proposed. Magnetic field distortion occurred due to internal environmental factors of the cube-satellite. This causes a fatal error in ADCS, two methods have been proposed to solve this problem. One is a method of compensating a magnetic field measurement that is distorted by temperature, current, and metal. The time-varying bias error was removed by modeling the magnetic field measurement distortions for temperature, current, and metal, respectively. In addition, the measurement noise of EKF was

set differently according to the operational scenario of the cube-satellite. Through this, an appropriate algorithm for the attitude estimation according to the magnetic field distortion has been developed. The other is a solution to the residual dipole moment caused by the current. The residual dipole moment is numerically modeled and reflected in EKF process noise. The proposed algorithm for magnetic field distortion was verified through simulation including the worst case magnetic field distortion, so that ADCS performance was predicted for the effect of magnetic field distortion in space.

Second, a design and constructing method of Helmholtz cage for HILS verification was proposed. To do this, the current-magnetic field relationship of Helmholtz cage was modeled and predicted the performance of Helmholtz cage through simulation. In addition, a Helmholtz cage, which generates a uniform magnetic field space covering the cube-satellite, was fabricated using CAD. To control the magnetic field of Helmholtz cage, the controller was designed to approximate the transfer function from the current-magnetic field model of Helmholtz cage and to classical control method. Using this, the HILS environment of the single axis ADCS was constructed by hanging the cube satellite in the inner space of Helmholtz cage. Then, HILS verification of ADCS was performed. Here, the nadir-pointing attitude was simulated by redefining the mean measurement of the magnetic field generated in the Helmholtz cage and the sunlight

simulated in the ground environment as the reference vector. Also, in the proposed HILS environment, a coordinate system is defined based on Helmholtz cage. From the defined coordinates, a simulation of the nadir-pointing in the ground environment was constructed and compared with the experimental results. Through the experimental results, the usefulness of the proposed method has been verified. The degradation of the estimation performance due to the magnetic field containing the statistical error characteristic in the ground environment, and the problem of the control performance deterioration due to small input torque of magnetorquer are solved. As a result, it is confirmed that the estimation performance and the control reliability of ADCS can be verified effectively compared with the existing method which does not use the Helmholtz cage.

Due to its simplicity and practicality, the proposed method is expected to be easily used for the verification of ADCS performance of a cube-satellite equipped with a magnetorquer only. Furthermore, it is expected that the ADCS performance will be improved by effectively solving the magnetic field distortion problem of the cube-satellite.

References

[1] H. Heidt, J. Puig-Suari, A. S. Moore, S. Nakasuka, and R. J. Twiggs, "CubeSat: A new Generation of Picosatellite for Education and Industry Low-Cost Space Experimentation," *AIAA/USU Conf. Small Satell.*, pp. 1–19, 2000.

[2] A. Chin, R. Coelho, R. Nugent, R. Munakata, and J. Puig-Suari, "CubeSat: The Pico-Satellite Standard for Research and Education," *AIAA Sp. 2008 Conf. Expo.*, no. September, pp. 1–11, 2008.

[3] J. Bouwmeester and J. Guo, "Survey of worldwide pico- and nanosatellite missions, distributions and subsystem technology," *Acta Astronaut.*, vol. 67, no. 7–8, pp. 854–862, 2010.

[4] S. Ni and C. Zhang, "Attitude determination of nano satellite based on gyroscope, sun sensor and magnetometer," *Procedia Eng.*, vol. 15, pp. 959–963, 2011.

[5] M. Reyhanoglu, C. Ton, and S. Drakunov, "Attitude Stabilization of a Nadir-Pointing Small Satellite Using Only Magnetic Actuators," in *IFAC Proceedings Volumes*, 2009, vol. 42, no. 19, pp. 292–297.

[6] D. M. Meissner, M. Romano, F. Approved, and O. M. B. No, "A three degrees of freedom test-bed for nanosatellite and cubesat attitude dynamics, determination, and control," Naval postgraduate school, 2009.

[7] M. Tassano, P. Monzon, J. Ramos, G. De Martino, and J. Pechiar, "a N I Nexpensive a Ttitude D Etermination S Ystem for the U Ruguayan C Ubesat , a Ntel S At," pp. 1–5, 2014.

[8] A. R. Walker, P. T. Putman, and K. Cohen, "Solely Magnetic Genetic/Fuzzy-Attitude-Control Algorithm for a CubeSat," *J. Spacecr. Rockets*, vol. 52, no. 6, pp. 1627–1639, 2015.

[9] J. Kim, Y. Jung, and H. Bang, “Linear time−varying model predictive control of magnetically actuated satellites in elliptic orbits,” *Acta Astronaut.*, vol. 151, no. November 2017, pp. 791–804, 2018.

[10] J. Li, M. Post, T. Wright, and R. Lee, “Design of Attitude Control Systems for CubeSat−Class Nanosatellite,” *J. Control Sci. Eng.*, vol. 2013, pp. 1–15, 2013.

[11] T. Inamori, K. Otsuki, Y. Sugawara, P. Saisutjarit, and S. Nakasuka, “Three−axis attitude control by two−step rotations using only magnetic torquers in a low Earth orbit near the magnetic equator,” *Acta Astronaut.*, vol. 128, pp. 696–706, 2016.

[12] Y. Kim, “Attitude Determination and Control of CubeSat using Magnetic Torquer and LQR Controller,” Seoul National University, 2015.

[13] M. Choi, “Sensor Calibration and Single−axis HIL Verification of ADCS for Low Earth Orbit Cube−satellite,” Seoul National University, 2017.

[14] J. Jang, “Attitude Determination and Control System for Low Earth Orbit CubeSat Considering Operation Senario,” Seoul National University, 2016.

[15] J. Jang *et al.*, “Development and Verification of LQG based Attitude Determination and Control Algorithm of Cube−satellite " SNUGLITE " using GPS and Multiple Sensors,” in *Proceedings of the 29th International Technical Meeting of The Satellite Division of the Institute of Navigation (ION GNSS+ 2016)*, 2016, pp. 3731–3739.

[16] M. Choi, J. Jang, S. Yu, O. Kim, H. Shim, and C. Kee, “Single−axis Hardware in the Loop Experiment Verification of ADCS for Low Earth Orbit Cube−Satellite,” *J. Positioning, Navig. Timing*, vol. 6, no. 4, pp. 195–203, 2017.

[17] M. Choi, S. Yu, O.-J. Kim, H. No, H. Shim, and C. Kee, "Development and verification of attitude determination and control algorithm for 'SNUGLITE' cube satellite," in *Proceedings of the 2018 International Technical Meeting of The Institute of Navigation, ITM 2018*, 2018, pp. 56–71.
[18] J. C. Springmann and J. W. Cutler, "Attitude-Independent Magnetometer Calibration with Time-Varying Bias," *J. Guid. Control. Dyn.*, vol. 35, no. 4, pp. 1080–1088, 2012.
[19] H. No, "Sensor Failure Scenarios and Corresponding Solutions of Three Axis Magnetometer Integrated GPS/INS UAV Navigation System," Seoul National University, 2017.
[20] J. C. Springmann, J. W. Cutler, and H. Bahcivan, "Magnetic Sensor Calibration and Residual Dipole Characterization for Application to Nanosatellites," *AIAA/AAS Astrodyn. Spec. Conf.*, no. August, pp. 1–14, 2010.
[21] H. E. Soken, S. i. Sakai, and R. Wisniewski, "In-orbit estimation of time-varying residual magnetic moment," *IEEE Trans. Aerosp. Electron. Syst.*, vol. 50, no. 4, pp. 3126–3136, 2014.
[22] T. Suehiro, *Satellite design methodology to suppress time-varying residual magnet effects on attitude for nano-satellites*, vol. 18, no. PART 1. IFAC, 2010.
[23] D. Gerhardt, "Small Satellite Passive Magnetic Attitude Control," University of Colorado, 2014.
[24] M. K. Quadrino, "Testing the Attitude Determination and Control of a CubeSat with Hardware-in-the-Loop," Massachusetts Institute of Technology, 2014.
[25] M. K. Prinkey *et al.*, "CubeSat Attitude Control Testbed Design : Merritt 4-Coil per axis Helmholtz Cage and Spherical Air Bearing," *AIAA Guid. Navig. Control Conf.*, pp. 1–12, 2013.
[26] H. Woo, O. Rico, S. Chesi, and M. Romano, "CubeSat Three Axis Simulator(CubeTAS)," *AIAA Model. Simul. Technol. Conf.*, no. August, pp. 1–8, 2011.

[27] A. Noureldin, T. B. Karamat, and J. Georgy, *Fundamentals of inertial navigation, satellite-based positioning and their integration*. 2013.
[28] George Siouris, *Aerospace Avionics Systems: A Modern Synthesis*, 1st ed. Academic Press, 1993.
[29] B. A. Earl, *Control of Spacecraft and Aircraft*. Princeton Universiy Press, 1994.
[30] M. D. SHUSTER and S. D. OH, "Three-axis attitude determination from vector observations," *J. Guid. Control. Dyn.*, vol. 4, no. 1, pp. 70–77, 1981.
[31] E. J. Lefferts, F. L. Markley, and M. D. Shuster, "Kalman Filtering for Spacecraft Attitude Estimation," *J. Guid. Control. Dyn.*, vol. 5, no. 5, pp. 417–429, Sep. 1982.
[32] M. Choi, S. Yu, O.-J. Kim, H. No, H. Shim, and C. Kee, "Development and verification of attitude determination and control algorithm for 'SNUGLITE' cube satellite," in *Proceedings of the 2018 International Technical Meeting of The Institute of Navigation, ITM 2018*, 2018, vol. 2018–Janua, pp. 56–71.
[33] D. J. Griffiths and C. Inglefield, *Introduction to Electrodynamics*. 2005.
[34] N. S. Nise, "Control system engineering, John Wiley & Sons," *Inc, New York*, 2011.
[35] I. Gaponov, D. Popov, and J. H. Ryu, "Twisted string actuation systems: A study of the mathematical model and a comparison of twisted strings," *IEEE/ASME Trans. Mechatronics*, vol. 19, no. 4, pp. 1331–1342, 2014.

국문요약

헬름홀츠 케이지를 이용한 저궤도 큐브위성 자세결정 및 제어시스템의 HILS 검증

본 논문에서는 자기토커를 구동기로 탑재한 저궤도 큐브위성에 대해, 지구지향 자세유지를 위한 자세결정 및 제어시스템의 성능검증 기법을 제안한다. 반작용휠을 탑재한 일반적인 위성과 달리, 공간적 제약을 가지는 큐브위성의 효과적인 운용을 위해 단순하고 저중량, 저전력의 자기토커만을 구동기로 탑재하여 지구지향 자세유지를 수행한다. 이를 위해, 먼저 큐브위성 자세에 대한 운동방정식을 중력구배토크, 그리고 자기토커의 쌍극자모멘트와 지구 자기장의 외적으로 산출되는 입력 토크에 대해 표현하고, 시스템에 유입되는 불확실성을 잡음원으로 취급하여 선형 시스템 모델을 얻는다. 또한, 태양과 자기장 모델로부터 기준벡터를 정의하고 태양 센서와 자기장 센서, 그리고 자이로스코프 측정치를 융합하여 큐브위성의 자세를 추정하는 확장 칼만 필터를 구성한다. 여기에, 주어진 선형 시스템과 입력에 대해 비용함수를 구성하고 최적해를 산출함으로서 지구지향 자세를 유지하는 LQR 제어기를 설계한다. 제안된 시스템의 성능을 검증하기 위해, 지상환경의 다양한 제약조건을 고려한 HILS가 수행되어야 한다. 하지만, 자기토커만 탑재한 큐브위성은 작은 입력토크, 지구 자기장 크기에 비례한 출력결정, 비연성 제어구동 등의 구동성능 한계로 인해 지상환경에서 전술한 시스템의 효과적인 성능 검증이 어렵다.

지금까지 큐브위성 자세결정 및 제어시스템의 성능검증은 대부분 운용의 안정성 확보를 위한 각속도 안정화, 지구 자기장 정렬에 의존한 수동제어 방식, 그리고 반작용휠을 활용한 지구지향 자세유지의 HILS가 연구되어 왔다. 자기토커만을 탑재한 자세결정 및 제어시스템의 HILS가 제안된 바가 있으나, 지상환경의 제약조건으로 인하여 성능검증에 한계가 있었다. 이와 달리, 제안되는 HILS는 기존방법의 한계를 보완하여 다양한 오차가 내포하는 환경에서 자기토커만을 구동기로 탑재한 큐브위성 자세결정 및 제어시스템의 성능검증에 목표를 두고 있다. 따라서 본 논문에서는 자기토커의 외부자기장 크기에 비례한 출력특성에 착안하여, 헬름홀츠 케이지를 이용한 큐브위성 자세결정 및 제어시스템의 HILS 검증기법이 제안된다. 즉, 지상환경에서 통계적 오차특성을 내포하는 자기장으로 인한 추정 성능저하와 외란에 취약한 자기토커의 작은 입력토크로 인한 제어 성능저하 문제를 헬름홀츠 케이지로부터 생성된 자기장 벡터를 제어함으로써 해결하고자 한다. 이를 위해, 비오-샤바르 법칙을 활용하여 헬름홀츠 케이지의 전류-자기장 관계를 모델링하고 큐브위성을 포함한 공간의 자기장 균일성을 확보할 수 있는 헬름홀츠 케이지를 제작한다. 또한 제시된 헬름홀츠 케이지의 전류-자기장 모델로부터 전달함수를 근사하고 고전제어기법을 활용하면 헬름홀츠 케이지의 자기장 벡터 제어기를 손쉽게 설계할 수 있다. 여기에, 헬름홀츠 케이지 내부공간에 큐브위성을 실에 매달아 단일축 자세결정 및 제어시스템 HILS 환경을 구성하고, 자세결정 및 제어시스템의 HILS 검증을 수행한다. 이때, 실내에 구축된 실험환경에서 GPS 측정치를 산출할 수 없으므로 모사된 태양광과

헬름홀츠 케이지에서 생성되는 자기장의 평균 측정치를 기준벡터로 재정의하여 지구지향 자세를 모사한다. 제시된 HILS 환경에서 헬름홀츠 케이지를 기준으로 좌표계를 정의하면, 지상환경에서 큐브위성의 지구지향 자세유지에 대한 시뮬레이션을 구성할 수 있다. 이러한 시뮬레이션 결과에 근거하여 실제 실험결과와 비교하면, 제안된 자세결정 및 제어시스템의 성능을 해석할 수 있다.

제안된 방법의 유용성을 확인하기 위해, SNUGLITE(Seoul National University GNSS Laboratory satelliTE) 큐브위성의 단일축 자세결정 및 제어시스템 HILS 검증이 제시된다. 제안된 방법은 지상환경에서 큐브위성에 대표적으로 탑재되는 자기토커만을 활용하여, 큐브위성의 지구지향 자세유지를 위한 자세결정 및 제어시스템을 검증할 수 있음을 보인다. 실험결과로부터 기존 방법의 지상환경 제약조건으로 인한 HILS 검증 한계를 헬름홀츠 케이지를 활용하여 보완함을 보인다. 또한, 헬름홀츠 케이지를 활용하지 않는 기존 방법과 비교하여 자세결정 및 제어시스템의 추정 성능 및 제어 신뢰성을 효과적으로 검증할 수 있음을 확인한다. 제안된 HILS 검증기법은 간결성 및 실용성으로 인해 다양한 임무수행을 위한 큐브위성의 자세결정 및 제어시스템 검증에 활용될 것으로 기대된다.

주요어: 큐브위성, 헬름홀츠 케이지, 자기토커, 자세결정 및 제어시스템, 확장 칼만 필터, LQR 제어기, HILS(Hardware In the Loop Simulation)
학번: 2017-24667

O the depth of the riches

both of the wisdom and knowledge of God!

how unsearchable are his judgments,

and his ways past finding out!

For who hath known the mind of the Lord?

or who hath been his counsellor?

Or who hath first given to him,

and it shall be recompensed unto him again?

For of him, and through him, and to him, are all things:

to whom be glory for ever. Amen.

Romans 11:33-36 (KJV)